Behaviour of Ni-Based Coating Alloys in Supercritical Water

by

Yunfen Qian
B.Eng., Mechanical, USST, 2004

A thesis submitted to
the Faculty of Graduate and Postdoctoral Affairs
in partial fulfillment of the requirements for the degree of

Master of Applied Science

in

Ottawa-Carleton Institute for Mechanical and Aerospace Engineering

Department of Mechanical and Aerospace Engineering
Carleton University
Ottawa, Ontario
Canada
September 2011

Your file Votre référence
ISBN: 978-0-494-83066-6
Our file Notre référence
ISBN: 978-0-494-83066-6

The undersigned recommend to
the Faculty of Graduate and Postdoctoral Affairs
acceptance of the thesis

Behaviour of Ni-Based Coating Alloys in Supercritical Water

Submitted by

Yunfen Qian
B.Eng., Mechanical, USST, 2004

in partial fulfilment of the requirements for the degree of
Master of Applied Science

Professor Xiao Huang, Thesis Supervisor

Professor Metin I. Yaras, Chair, Department of Mechanical and Aerospace Engineering

Carleton University
September 2011

Abstract

Corrosion resistance is a key performance factor for engineering materials used in the supercritical water-cooled reactors proposed as one of the Generation IV nuclear energy systems. This thesis reports the preliminary findings of several potential coating materials after corrosion testing carried out under supercritical water condition.

Five nickel based coating alloys with various Al and Cr contents and surface preparation methods were evaluated. It was found that the corrosion resistance can be enhanced by the addition of aluminum and chromium into nickel-based alloys. Also, surface preparation methods influenced the corrosive behaviour greatly.

Additionally, bare and NiCrAlY coated IN625 and 304SS were also tested and the weight and surface microstructure changes were assessed. IN625 is more resistant to corrosion than 304SS in general. NiCrAlY coating showed excellent corrosion resistance and the heat treated NiCrAlY had even greater corrosion resistance due to the formation of alumina on the surface. The combination of NiCrAlY coated on IN625 could be a promising candidate for future SCWRs application.

Acknowledgements

This thesis is very special for me. The past two years has been both educational and enlightening. Frankly, I went through a tough process. I am fortunate enough however, to have had people in my life who provided extensive support and encouragement. I would like to take this opportunity to express my sincere gratitude to my supervisor, Professor Xiao Huang, for both her patience and kindness. Dr. Huang provided me with guidance and opportunity above and beyond the call of duty.

The full support from my parents has been one of the driving forces for me to keep going, to challenge, and to struggle. I have to say I am nothing without their love.

Also, my thanks must be extended to: Austin Selvig, Feng Gao, Fred Barrett, Nancy Powell, Christie A. Egbert, Stephan Biljan, Alex Proctor, Kevin Sangster, Steve Truttmann and Prof. Rong Liu of the Department of Mechanical and Aerospace Engineering here at Carleton; as well as Dr. Jianqun Wang of SEM laboratory at Carleton. This thesis would not be possible without their help. Sometimes, just a greeting or smile can make me, an ordinary foreign student, feel warm in this unfamiliar country.

Finally, I would like to thank all the new friends I have made in this great country. Particular thanks need to be conveyed to Paul Gallien. He and his family let me experience the Canadian culture of the most. Also, he helped me with the proofreading of this thesis.

Table of Contents

List of Tables

List of Figures

List of Appendices

Nomenclature

ε	Dielectric Constant
μm	Micrometer
°C	Degrees Celsius
304 SS	Stainless Steel 304
AECL	Atomic Energy of Canada Limited
BWR	Boiling Water Reactor
CANDU	Canada Deuterium-Uranium Reactor
CANMET	CANMET Energy Technology Centre
CERT	Constant Extension Rate Tests
CLT	Constant Load Tests
CP	Critical Point
CSLB	Coincidence Site Lattice Boundaries
DO	Dissolved Oxygen
dpa	Displacements Per Atom
E	Electrochemical Potential
EDS	Energy-Dispersive X-ray spectroscopy
FIB	Focused Ion Beam
F-M Steel	Ferritic-Martensitic Steel
ft-lb	Foot Pound-Force
GIF	Generation IV International Forum
H^+	Hydron

HDSCW	High Density Supercritical Water
IC	Intergranular Corrosion
IGSCC	Intergranular Stress Corrosion Cracking
IN 625	Inconel 625 Alloy
LDSCW	Low Density Supercritical Water
LWR	Light Water Reactor
MPa	Megapascal
NRCan	Natural Resources Canada
OH^-	Hydroxide Ion
ppb	Part Per Billion by Mass
ppm	Part Per Million by Mass
psi	Pound-Force Per Square Inch
PWR	Pressurized Water Reactor
SCC	Stress Corrosion Cracking
SCFP	Supercritical Water Fossil-Fired Plant
SCW	Supercritical Water
SCWO	Supercritical Water Oxidation
SCWRs	Supercritical Water-Cooled Reactors
SEM	Scanning Electron Microscope
STEM	Scanning Transmission Electron Microscope

1. Introduction

It has been proposed that a supercritical water-cooled reactor (SCWR) be used as part of the development of next generation (Gen IV) nuclear power generation with the operating conditions outlined in Figure 1-1 [1, 2, 3]. The primary objective is to increase the plant efficiency and to reduce overall footprints. The supercritical water turbine cycle can reach a thermal efficiency of over 40% as compared with an advanced boiling water reactor (BWR) system with 34% maximum thermal efficiency [4]. Also, since the specific volume of supercritical water is small, the size of the main components, such as the turbines, can be made even more compact. Additionally, the recirculation system, steam generators and steam-water separators used in the traditional steam engine plant, can be eliminated due to the absence of a phase change in the supercritical regime.

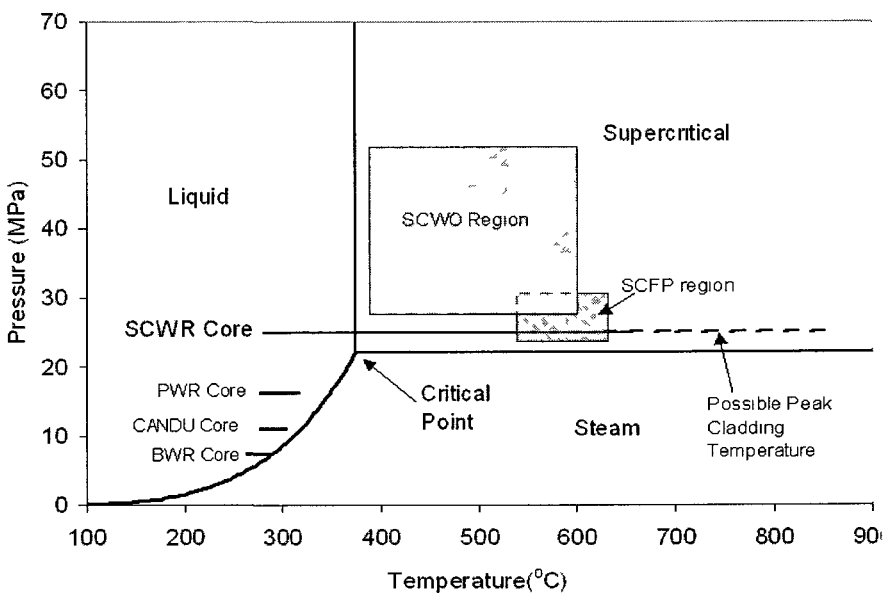

Figure 1-1 CANDU SCWR operating region [2].

The use of supercritical water (SCW) presents challenges to the fluid containment materials due to corrosion concerns. Material's behaviours in SCW change with fluid properties significantly. Most metal oxides show increased solubility in either acidic or alkaline SCW fluid and any increase in the ionic character of water will cause an increase in corrosion [5]. The solubility of oxygen in SCW is another consideration. Increased oxygen concentration increases the oxidizing power of the fluid. The corrosion rate of different materials is also sensitive to the density of SCW. The corrosion rate has been correlated to the density of the water. As such potential materials must be tested under SCWR conditions before utilization.

Although SCW has been used as the working fluid in fossil fuel plants and as a high efficiency solvent for organics, a supercritical water-cooled nuclear power plant presents increased materials challenges due to the effects of radiation on both the alloy and on the coolant; water radiolysis results in the production of oxidizing species which can lead to increased corrosion. Ferritic-Martensitic steels, austenitic stainless steels and nickel based alloys are some of the candidate materials proposed for a SCWR [5, 6]. However, most of these materials suffer from excessive corrosion at the high temperatures proposed for the CANDU SCWR concept.

The corrosive effect of supercritical water on a number of potential coating materials (NiCr, NiAl, NiCrAl and NiCrAlY) was investigated in this study in addition to NiCrAlY plasma coated 304 SS and IN 625 in SCW at 500°C.

2. Literature Review

The following sections introduce some of the important topics related to supercritical water properties, the design of SCWRs and engineering materials that could be used in SCWRs.

2.1 General Introduction

With the ongoing expansion and the industrialization of the world's population comes the constant seeking of reliable and sustainable energy resources. For the earth to support its developing population we must increase the production of energy and use energy sources more efficiently. Currently nuclear energy holds the highest potential to partly replace the use of fossil fuels and fill the energy demand. It also significantly reduces the environmental impact of current electricity generation and provides a larger diversity of electricity generation that enhances energy security.

Several developed and developing countries are using nuclear energy as their essential and valuable source of energy. While increasing amount of energy comes from nuclear power (13% of world's electricity generated from nuclear power as of 2008 [7]), challenges still exist to further the large-scale use of nuclear energy, safely and efficiently.

A decade ago, experts from some countries, including Canada, have already launched a program aimed at building a new state-of-the-art generation of nuclear energy system (Generation IV)[4, 8]. The Generation IV International Forum (GIF) has selected six advanced systems as the most promising directions for future research. The six systems

are summarized in Table 2-1 [8]. From both technical and practical point of view, these systems could fulfill the essential goals of Generation IV nuclear energy system program in four areas: sustainability, economics, safety and reliability, as well as proliferation resistance and physical protection. Enormous challenges, however, remain.

Table 2-1 Overview of six Generation IV systems [8].

System	Neutron Spectrum	Coolant	Temperature °C	Fuel Cycle	Size (MWe)
VHTR (very-high-temperature reactor)	Thermal	Helium	900-1000	Open	250–300
SFR (sodium-cooled fast reactor)	Fast	Sodium	550	Closed	30–150, 300–1500 1000–2000
SCWR (supercritical water-cooled reactor)	Thermal fast	Water	510–625	Open/ closed	300-700 1000–1500
GFR (gas-cooled fast reactor)	Fast	Helium	850	Closed	1200
LFR (lead-cooled fast reactor)	Fast	Lead	480–800	Closed	20–180 300–1200 600–1000
MSR (molten salt reactor)	Fast thermal	Fluoride salts	700–800	Closed	1000

Considering currently successfully operated CANDU technology, Canadian researchers are collaborating in the development of Supercritical Water-cooled Reactors (SCWRs) with European, Japanese and Chinese specialists. One of the highlights of the proposed SCWRs is the surprisingly increased plant efficiency. The supercritical water turbine cycle can reach a thermal efficiency of over 40% (recent research showed it might be more than 50%) compared with a contemporary advanced boiling water reactor (BWR) system with a maximum of 34% efficiency [1]. Also, since the specific volume of

supercritical water is small, the size of the main components, such as the turbines, can be made much more compact. Additionally, the recirculation system, steam generators and steam-water separators used in the traditional steam engine plant, can be eliminated due to the absence of a phase change in the supercritical regime [1] (Figure 2-1 [9]). All these benefits indicate that the electricity can be generated in a relatively low cost through the use of SCWRs.

The concept of supercritical water (SCW) is not new; in fact, it has already been used in, to some extent, several fossil fuel power plants (SCFP) [10, 11] and supercritical water oxidation (SCWO) reactors to destroy hazardous wastes [12]. The technical gap, other than materials, between SCWRs and existing Light Water Reactors (LWRs) is not that great [13].

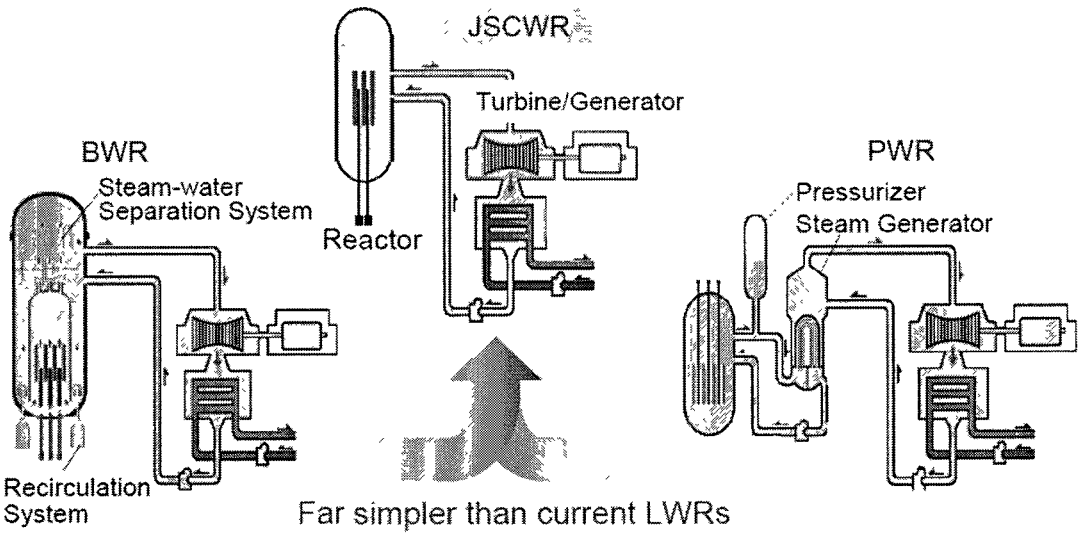

Figure 2-1 Schematic of proposed Japanese SCWR [9].

The use of SCW in nuclear power plant presents challenges to the fluid containment materials due to corrosion concern. Furthermore, material's behaviours in SCW change with fluid properties significantly. Most metal oxides, used to protect the underlying substrate, show increased solubility in either acidic or alkaline SCW fluid; therefore, a surge in the ionic character of water will cause an increase in corrosion. The solubility of oxygen is another consideration. Increased oxygen concentration increases the oxidizing power of the fluid. The corrosion rate of different materials is also sensitive to the density of SCW. More detailed descriptions of SCW properties are discussed in the following sections.

Although SCW has been used as the working fluid in fossil fuel plants and as a high efficiency solvent for organics, a SCW nuclear power plant presents different type of material's challenges due to the effects of radiation on both the alloys and coolants. Water radiolysis results in the production of oxidizing species which can lead to increased corrosion in SCW containment materials.

The criteria of selection SCWR materials include tensile and creep rupture properties, corrosion behaviour and successful operation in nuclear reactors. Previous studies have revealed several types of materials that are suitable for moderate supercritical water conditions. Ferritic-Martensitic steels, austenitic stainless steels and nickel based alloys are some of the candidate materials proposed for a SCWR [5, 6, 10]. Nickel based alloys show a low general corrosion in steam environment and their relatively high creep strength makes them good candidate for SCWRs use. Furthermore, coating is being

considered for its application as protective over-layer for stainless steels and superalloys due to its flexible composition and preferable oxidation resistance.

2.2 Physical and Chemical Properties of Water

Water, the most abundant liguid on our planet, has been studied and used widely near ambient conditions. Much less is understood about water under extreme states, such as those encountered in the supercritical region (see Figure 2-2). A supercritical fluid is any substance at a temperature and pressure beyond its Critical Point (CP), where specific liquid and gas phases do not exist. For water, the CP is temperature at 374.1°C and a pressure of 22.1MPa. Normally, there is no further phase transformation above CP and the matter is considered to be neither liquid nor gas, but rather a homogenous supercritical fluid [14]. For example, it exhibits both liquid-like and gas-like characteristics, which can diffuse through solids like a gas and dissolve substances like a liquid. Due to this unique feature, SCW exhibits many peculiar and exceptional properties. Additional properties such as the density, hydrogen bonding, ionic product (pH value) and oxygen solubility will be discussed in the following sections.

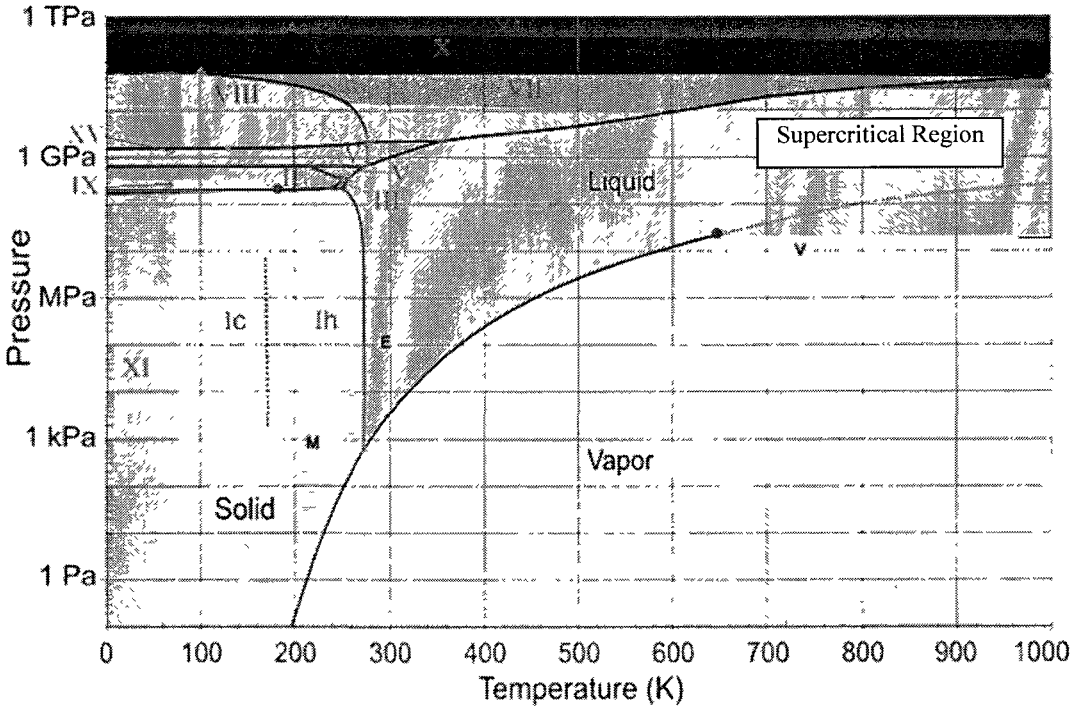

Figure 2-2 Phase diagram of water [15].

2.2.1 Density

The density of water, as expected, decreases gradually with increasing temperature around ambient conditions. Nevertheless, it drops rapidly near the CP point. Thereafter, the decline of density turns to moderate after entering into the supercritical regime as showed in Figure 2-3.

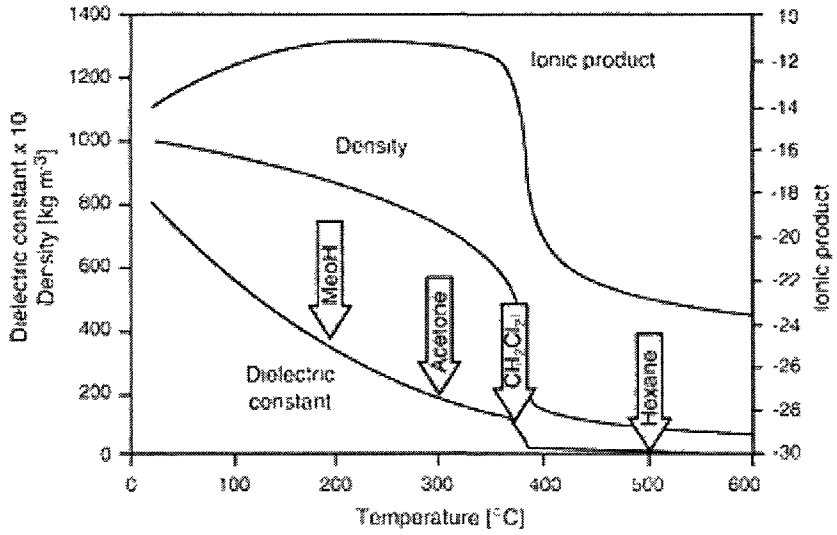

Figure 2-3 Physical properties of water vs. temperature at 24 MPa. Dielectric constants of typical organic solvents at room temperature are also indicated [16].

Although supercritical fluids do not go through any further phase transformation above the critical temperature and pressure, physical properties such as density, ionic product or dielectric constant can differ dramatically from changes in pressure [14]. The volumes of these properties are highly dependent on pressure [17]. To some extent, it is attractive that the density of SCW can be controlled between gas-like and liquid-like values by varying its pressure and temperature (which determines the density) [18]. This character of SCW can be used in predicting the corrosion rate under these conditions: the corrosion rate can be approximated as a simple function of the density of the water and plots of density versus temperature (Figure 2-4) can be taken as a rough approximation to corrosion rates versus temperature [19]. Higher corrosion rates occur when the density of SCW exceeds approximately 250 kg/m^3. As shown in Figure 2-4, the availability of a wide range of the density is the most appealing characteristic of SCW [20].

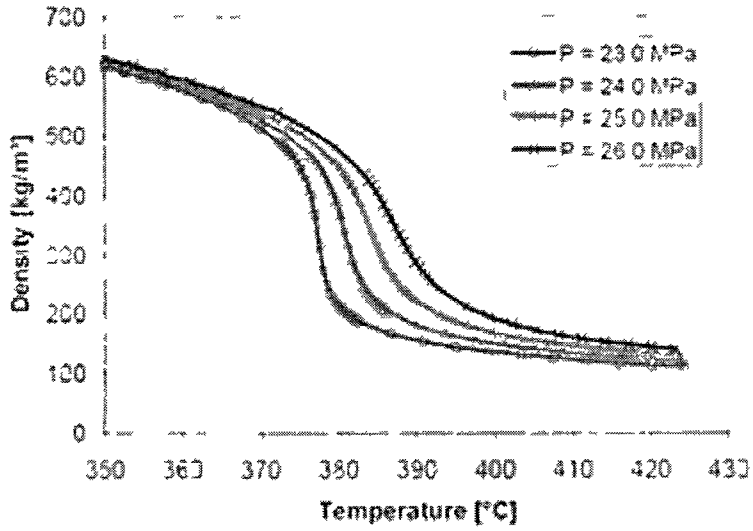

Figure 2-4 Density as a function of temperature at various pressures [19].

2.2.2 Dielectric Constant and Hydrogen Bonding

Water has a strong polarity at ambient temperature as a result of a dipole caused by significant difference in the electro-negativity of hydrogen and oxygen atoms. The dielectric constant (ε) is used to reflect the extent of this polarity [14]. Water molecules form hydrogen bonds amongst the hydrogen atoms and the electronegative atoms, oxygen. The unique behaviours exhibited by water are believed to be caused by the hydrogen bond. For instance, intermolecular hydrogen bonding is responsible for the high boiling point of water compared to the other hydrides that have no hydrogen bonds [21]. The polarity of water molecules can also influence the solubility of different salts or inorganic compounds in water [22].

With the increasing temperature and pressure, intermolecular interaction of the hydrogen bonding decreases considerably as a result of lower density and intermolecular force. The

degree of hydrogen bonding at 300°C is only 25 percent of that in room temperature. When it comes to supercritical region (at 400°C), almost all hydrogen bonding is broken down [18, 23, 24]. As a result of less hydrogen bonding and lower density, the polar effect of water diminishes remarkably, which corresponds with the dramatic drop of dielectric constant. Interestingly, SCW behaves more like a non-polar rather than a polar solvent, permitting solution of most organic compounds and oxygen. On the other hand, with rising temperature, polar inorganic salts are no longer soluble and start precipitating, which have detrimental impact on SCWR operations since corrosion products may start to deposit on components.

2.2.3 Ionic Product and the pH value

The amount of ionic product, which stands for the ions present in a specific solution, falls down sharply near CP as shown in Figure 2-3. Liquid water self-dissociates into H^+ and OH^- ions under ambient conditions. The equilibrium is an endothermic reaction and thus the production of ions is favoured by increased temperature. The overall pH value remains stable at 7 and is considered both acidic and alkaline. The amount of ionic product is influenced by the temperature just like other physical properties; meanwhile it is driven by the pressure as well [5, 25]. The ionic product of high-temperature water with respect to pressure is shown in Figure 2-5. At low pressures, water behaves as a non-polar solvent with low self-dissociation while at high pressures it can increase the ionic product [5]. With the increase of ionic product, more mineral acids or bases may be formed which can affect the pH value of the solvent and make a difference on corrosion properties accordingly.

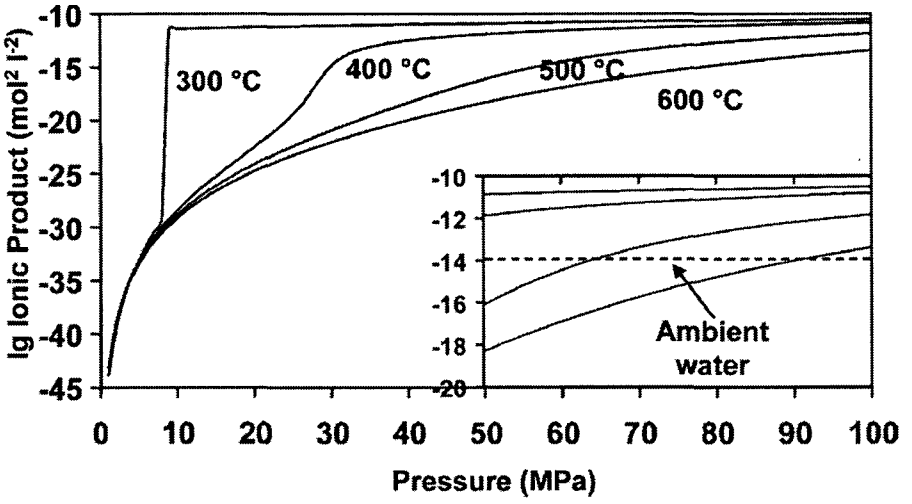

Figure 2-5 Ionic product of high-temperature water at different temperatures versus pressure [5].

2.2.4 Oxygen Solubility

SCW is a fluid possessing a full solvency for most gases, including oxygen [26]. The concentration of oxygen in SCW has been found to influence the thickness and stability of the protective oxide layer on many metals and alloys upon being immersed in SCW environment [5]. It is known that high solubility of oxygen increases the oxidizing power of SCW thus affecting the corrosion resistance of some materials.

All above characteristics can be adjusted by a change in pressure or temperature which is the most useful feature and main interest of SCW. A slight modification of temperature and/or pressure could have a drastic effect on the physical and chemical properties of the water. These special characteristics present challenges to finding the candidate materials which can be used in SCWR with varying temperature and pressure.

2.3 Corrosion Mechanisms and Factors

It is the integrity of the protective oxide layer which plays an important role in the corrosion properties of metals or alloys in SCW. The formation, morphology, and composition of surface oxides relies on the SCW conditions. At room temperature, a protective layer might be thermodynamically stable. It can, however, become unstable or active under supercritical water conditions leading to dissolution or subsequent re-formation of the oxides [5]. The effects of test condition will be further discussed in the following sections.

2.3.1 Effects of Temperature and Pressure

As mentioned before, density, ionic product and hydrogen bonding of water decrease rapidly near the critical point. It is to be pointed out that the curves presented in Figure 2-3 were generated assuming temperature as the only variable while other solution parameters remain constant. Exposure to SCW at 500°C might yield a lower corrosion rate than exposure to subcritical water at 300℃ due to the changes in the physical and chemical properties of water [5, 25]. The protective oxide layer, however, may change due to the exposure temperature. Specifically, for example, stainless steel alloys are normally protected by an amorphous chromium oxide layer at ambient conditions. Under higher exposure temperatures, this oxide can be replaced by a crystalline Cr (III) based oxide layer, leading to increased dissolution of the original protective oxide layer [5, 25].

It is well known that pressure has a strong correlation with the corrosion rates of metals or alloys under supercritical conditions [5]. An increase in pressure can increase the corrosion rate and consequently result in rapid dissolution of the protective layer [5].

2.3.2 Effect of pH value

The pH value is another key factor which can influence the dissolution of the protective oxide film. Normally, the effect of pH value on the oxides can be determined using a Pourbaix Diagram [27], which relates the pH value to electrochemical potential (in Volts). An example of a Pourbaix Diagram is showed in Figure 2-6. The diagram displays the 'passive region' of the oxides under a constant temperature. This envelope-like zone may shift or change shape based on the temperature [5].

The pH values that are either higher or lower than the 'stability island' can lead to dissolution of the protective oxide film. Experimental results have shown that chromium oxides had a minimum dissolution rate under neutral or slightly alkaline conditions while nickel oxides appeared to have the highest dissolution rate among iron, chromium and nickel oxide films [5, 28].

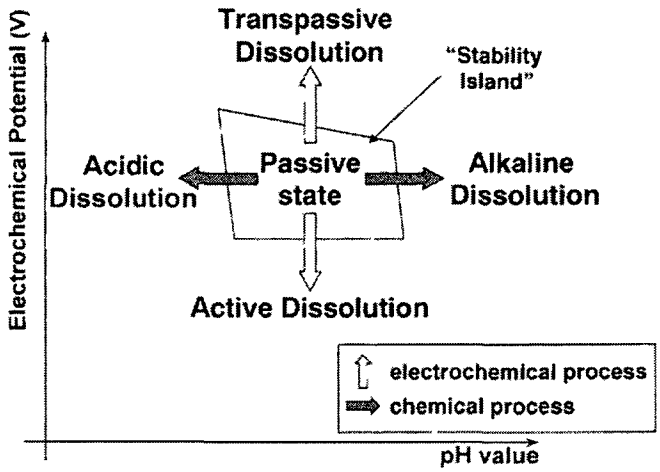

Figure 2-6 "Stability Island" of a protective oxide and principle mechanisms of dissolution [5].

By understanding this Pourbaix Diagram, actions can be taken to minimize the total corrosion effect, i.e., to ensure the protective oxide film remains intact. Figure 2-7 demonstrates one of the strategies used for reducing corrosion is to change the pH value or electrochemical potential (E). The chromium oxide, for example, stays functional at low pH and low potential value in A-region on the figure. The chromium oxide layer experiences transpassive dissolution with an increase in the potential (E) beyond then stable A-region while the nickel oxide would go through a chemical dissolution beyond C-region [5]. For Ni-Cr alloy, the pH value should be raised to reach C-region if the electrochemical potential is be increased beyond A-region to ensure that nickel oxide could act as an effective protective layer.

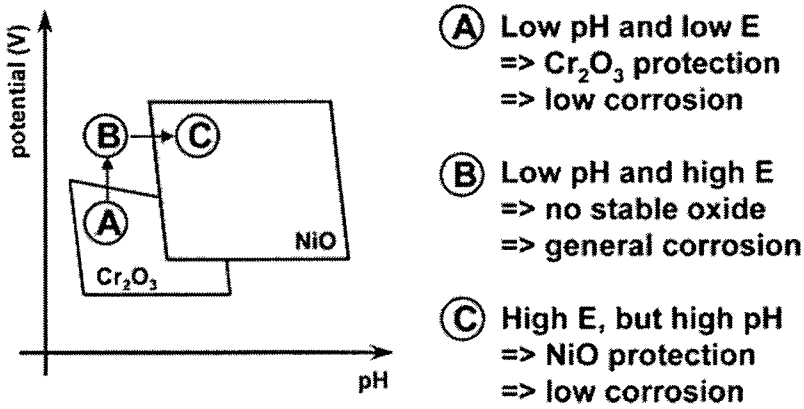

Figure 2-7 Stability Islands of chromium and nickel [5, 29].

2.3.3 Effects of Dissolved Oxygen

The oxidizing power of the solution is highly dependent on the concentration of dissolved oxygen. The concentration of dissolved oxygen in the oxidizing fluid is an important parameter which plays a key role on the integrity and the development of surface oxides [30]. For instance, Figure 2-8 shows that the morphology surface oxides can be different due to exposure at different concentrations of dissolved oxygen. Referring to this figure, the T91 steel sample exposed to higher oxygen concentration (b) displayed finer oxide grains with a larger number of interconnected pores while sample (a) immersed in lower oxygen concentration had larger pores in the surface oxide. Increased porosity and the occurrence of more fine pores might promote oxygen ion diffusion leading to further oxidation of the base metal and thus producing a thicker, unstable oxide layer in sample (b). It is difficult to predict the weight gain tendency with varied dissolved oxygen concentrations due to the thin nature of the oxide film. In one case, an initial decrease of weight gain was observed with increasing oxygen level until reaching certain oxygen

concentration before the weight gain increases. This upsurge was possibly due to the formation of a denser oxide layer and hematite layer at high oxygen level [31].

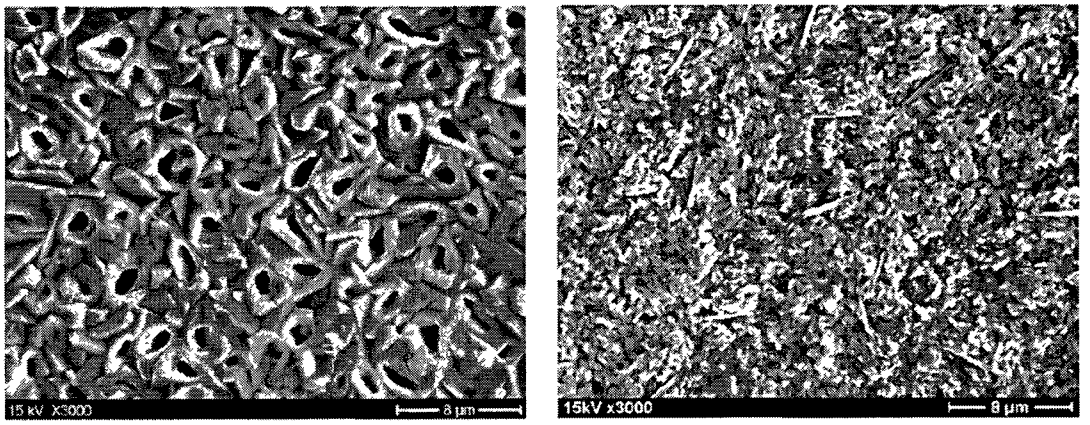

Figure 2-8 SEM image of oxide products after exposure to SCW at 500℃ (a) T91 in 25ppb DO SCW for 505hr (b) T91 in 2ppm DO SCW for 503hr [30].

2.4 Surface Preparation

In addition to the impact of fluid properties and material compositions on corrosion behaviour as described in literature review section, surface preparation has also shown to influence the corrosion behaviour of materials. In a study carried out by Guzonas [3], it was demonstrated that surface finish was one of the most important factors controlling the weight change when 304 SS was tested under SCW conditions. The water density and chemistry were found to be secondary. It is therefore another focus of this study to further examine the influence of different surface preparation methods.

2.5 Possible Materials for SCW Application

Ferritic-Martensitic (F-M) steel, Austenitic steel and Nickel based alloys are three classes of candidate materials considered for use in SCWRs. These alloys can also be coated to improve corrosion resistance. The following sections will describe the general corrosion behaviour, mechanical properties and radiation effect for each of these alloys.

2.5.1 Ferritic-Martensitic Steel

Ferritic-Martensitic steels have the lowest cost but also have lower working temperature due to over tempering [32]. They have low neutron absorption rates, good radiation resistance and they do not swell under radiation. F-M steels are austenized first, and then quenched and heat treated at 760℃ to convert a large portion of the martensite to ferrite. This gives a good balance of strength and toughness. F-M steels have the largest weight gain and oxide growth rate. However, this oxide is quite stable and does not spall. At low dissolved oxygen (DO) concentration (up to 300 ppb), a two phase oxide layer will form consisting of an outer layer of Magnetite and an inner layer of $(Fe, Cr)_3O_4$ spinel as shown in Figure 2-9. Since it is desirable to reduce the oxide layer thickness in order to reduce metal loss and insulation of the control and water rods, increased chromium content has been looked at. In one case an increase of 3% Cr decreased the oxide layer thickness by 25% [31]. In another test it was shown that the implantation of small amounts of Yttrium decreased the oxide layer thickness by about 50% [31]. While the growth of thick oxides is limiting the usage of F-M steels in reactors it can be clearly seen that with proper alloy modification this oxide layer can be reduced.

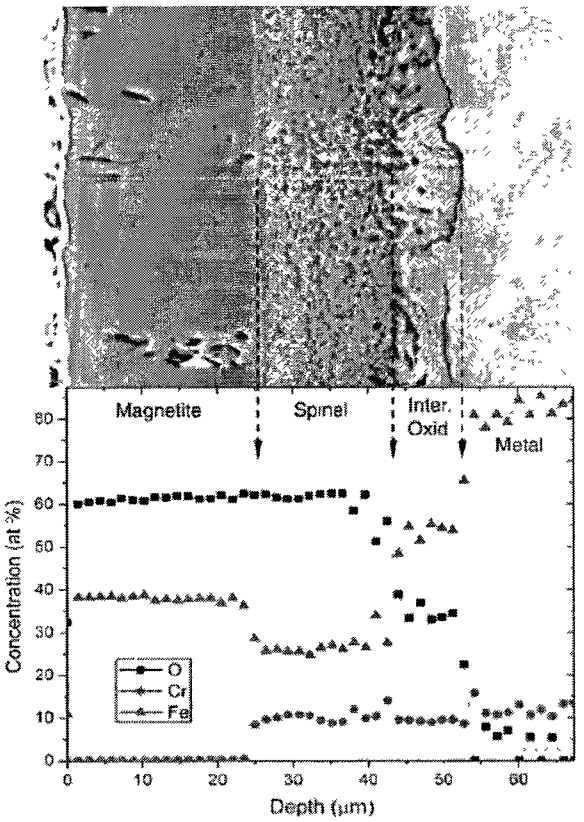

Figure 2-9 Cross-section image and EDS of HCM12A exposed to 600°C SCW with 25ppb DO for 1026h [31].

Another issue facing F-M steels is radiation hardening. A typical F-M alloy (T91), after being irradiated with a dose of 9 displacements/atom (dpa), showed a large increase in yield strength and a decrease in ductility at temperatures less than 450°C [33]. Above this temperature, the hardness of the metal was relatively unchanged after irradiation. F-M steels also suffered from radiation embrittlement. It was observed that the maximum energy absorbed by a Charpy V-notch specimen decreased by half (in the ductile region) after saturation with neutron radiation. And the ductile to brittle transition temperature increased from about 0°C to 150°C. The metal would be more vulnerable during re-start-

up and shut-down for maintenance as transient temperatures range from room temperature to operating temperature [31, 33, 34].

2.5.2 Austenitic Stainless Steel

Austenitic stainless steels are being considered for SCWRs due to their higher creep resistance, improved corrosion resistance over F-M steels, and their better radiation performance over nickel based alloys. However, austenitic stainless steels have many problems that still need to be overcome. They usually form a three-layer oxide which consistes of a layer of spinel covered with magnetite then hematite as shown in Figure 2-10. However, the layer thickness is much thinner and the magnetite and hematite layers are less uniform and contain more pores [31]. It has been reported [35] that many Austenitic stainless steels suffer from oxide spallation (see Figure 2-11) which could damage components downstream. Grain boundary engineering, which was performed in a controlled sequence of thermomechanical processing steps (rolling and annealing) with the goal of achieving a high volume fraction of coincidence site lattice boundaries (CSLB) in a material, of a certain austenitic alloy, 800H, resulted in improved oxide layer cohesion [36].

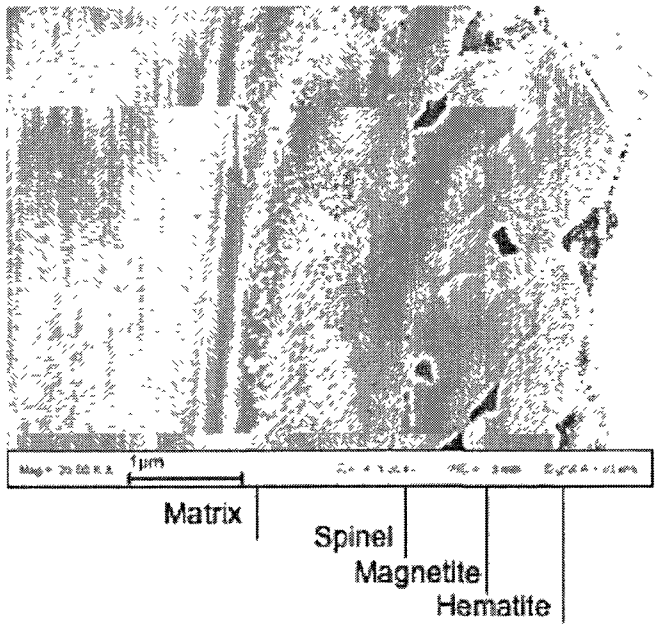

Figure 2-10 Cross-section of oxide formed on Alloy 800H exposed to 500 °C SCW with 25 ppb dissolved oxygen concentration for 505h [31].

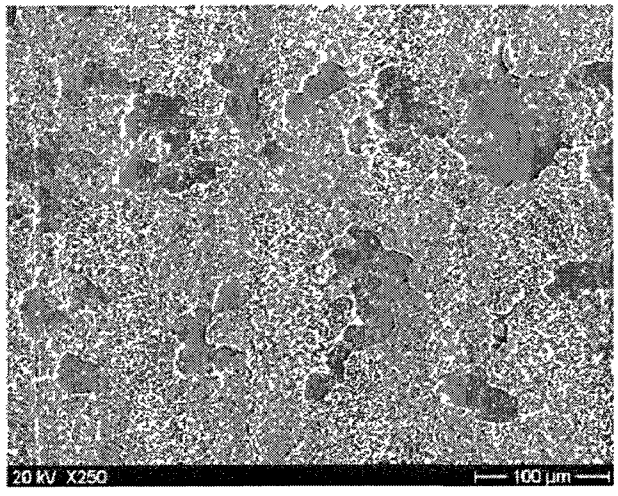

Figure 2-11 SEM morphology of D9 alloy sample after exposure to 2000 ppb DO SCW at 500 °C for 503 h [35]. (A typical spallation for austenitic alloys)

Austenitic stainless steels are also susceptible to stress corrosion cracking, typically Intergranular Stress Corrosion Cracking (IGSCC). It has been observed that the degree of this cracking increased with increasing water temperature and pressure. Also it was found that irradiation at high temperature increases the SCC substantially based on test results from constant extension rate tests (CERT) [31]. However, under constant load tests (CLT), which resemble service condition more closely, at high DO, no cracking occurred at all [31]. Some austenitic stainless steels show extreme swelling when irradiated (on the order of 15%), whereas F-M steels show very little (<1%). The austenitic alloys have higher neutron capture and lower thermal conductivity as well. Radiation also depletes Cr from the grain boundaries, increasing the susceptibly to intergranular corrosion [37].

2.5.3 Nickel Based Alloys

Nickel based alloys can be chosen for SCWR applications (out of the core components). Their corrosion rate and oxide layer growth rate are almost an order of magnitude smaller than those of the steels. Nickel based alloys also have the advantage of greater creep strength. However, these alloys also have disadvantages. They are higher in cost and poor in irradiated performance. Pitting corrosion has also been observed in these alloys. Nickel based alloys are also very susceptible to SCC. This susceptibility has been explained by segregation of alloy elements at the grain boundaries and possibly the expansion of oxidizing carbide particles within these grain boundaries [37]. This SCC susceptibility in Nickel based alloys is much higher than that of F-M steels. Nickel based alloys have particularly poor performance under neutron or proton radiation as they have higher

neutron absorption and low coefficients of heat transfer, making them a poor choice for reactor cladding. Furthermore, irradiation of Ni-based alloys also causes swelling, radiation embrittlement, and further increased susceptibility to stress corrosion cracking. These alloys have also been shown to produce Helium when irradiated, and are susceptible to Helium embrittlement (steels produce Helium as well but approximately a quarter of what is produced by nickel alloys) [34]. Certain alloying elements, such as Boron 11, can be added in nickel to reduce the formation of Helium. As such, nickel based alloy are more suitable for our-of-core components such as piping or turbine blades due to their high temperature strength, creep resistance and corrosion resistance in SCW [31, 33].

2.5.4 Coatings

One potential method for improving corrosion resistance, without sacrificing mechanical or irradiation properties, is by the application of a corrosion resistant coating to the surface of the material. Many iron, nickel and aluminum based coatings have been tested in steam environments and have shown good adhesion, thin, stable oxide formations and resistance to cracking although they have not yet been tested in irradiated environments. One coating that shows particularly good properties in the literature is Ni20Cr. Since HVOF deposited Ni20Cr shows no coating degradation or substrate attack and a very thin protective Cr_2O_3 layer on the coating surface after 20000h of exposure to steam at 650°C [38, 39]. Pack aluminizing of a nickel base alloy IN625, showed an increased corrosion resistance after 50h of being oxidized in air at 1000°C and 1100°C [40], whereas pack aluminizing and slurry coatings on steel substrates were found to be detrimental due to

the inward diffusion of aluminum towards the substrate rather than outwards during the diffusion heat treatment in argon at 700°C for 10h [39].

2.6 Summary

Based on foregoing literature review, it is apparent that there is no single alloy available commercially that can withstand the effects of all feed types under SCWR condition. As such, this research program was undertaken to examine various coatings for both nickel based alloys and stainless steels and assess their corrosion resistance in SCW.

3. Thesis Objectives and Scope

Based on the literature survey, it can be concluded that coatings are needed to protect the alloys used to construct SCWR. Since literature has indicated that Al_2O_3 showed superior corrosion resistance in SCWO environment [41, 42], Addition of Al in coating compositions was need. Also, Cr is known to provide corrosion resistance to stainless steels, Cr will also be included into the compositions examined in this study. Thus, gradual addition of Al, Cr and Al+Cr were incorporated into nickel based alloys to see how these elements effect corrosion resistance of the alloys in SCW. Additionally, NiCrAlY are commonly used in aero engines as corrosion resistant coatings, NiCrAlY will also be tested in this study accordingly.

The objective of this particular thesis is first to design a system capable of reaching SCW conditions and second, to test potential materials and coatings which can be used in Generation IV SCWRs.

In order to facilitate coating selection and development, bulk samples are first tested in SCW to identify the ideal coating composition. Since the corrosion behaviour is also dependent upon surface preparation methods, several surface preparation methods are used including grinding, polishing and heat treatment. Following the initial bulk sample test (also termed as button samples), a plasma spray coating process will be developed using the selected coating composition. The plasma sprayed overlay coating samples will be tested in supercritical water. The results will be summarized to provide suggestions for future material and coating development for SCWR applications.

4. Materials and Experimental Procedures

The following section describes the alloys used in this thesis and the experimental system and procedures.

4.1 Alloy Compositions

This thesis focuses on various nickel based alloys to determine the potential coating composition(s). The compositions for both bulk alloys (cut to button-like) and thermal sprayed coating are summarized in the following sections.

4.1.1 Button samples

A total of five 12.7 mm (0.5") diameter rods were fabricated by Sophisticated Alloys Inc. Each rod was cut into a number of button samples. These five materials have the compositions Ni20Cr, Ni5Al, Ni50Cr, Ni20Cr5Al and Ni20Cr10AlY (Table 4-1). Different compositions were selected to independently examine the effect of Cr and Al on the corrosion behaviour of nickel-based alloys in SCW.

Table 4-1 Compositions of five bulk alloy materials.

Composition	Ni	Cr (wt%)	Al (wt%)	Y (wt%)
Ni20Cr	Bal.	20	0	0
Ni5Al	Bal.	0	5	0
Ni50Cr	Bal.	50	0	0
Ni20Cr5Al	Bal.	20	5	0
Ni20Cr10AlY	Bal.	20	10	1

4.1.2 NiCrAlY coating samples

Austenitic Stainless steel 304 (304 SS) and Inconel 625 (IN 625) (McMASTER-CARR, USA) were used as substrate materials for this study. IN 625 was cut into strips measured 70 mm x 20 mm x1.5 mm while 304 SS were cut into strips of 35 mm x 12 mm x 1.5 mm. Both materials were coated with NiCrAlY coating (NI343, Praxair Surface technologies, Inc.) using plasma spray process (Axial III APS system, Northwest Mettech). Both nominal and measured compositions by EDS are shown in Table 4-2.

Table 4-2 Compositions for 304 SS, IN 625 and NiCrAlY (wt%).

	Ni	Cr	Mn	Si	Nb	Mo	Fe	Ti	Al	Y
304 SS (ref.)	8-10	18-20	2	1	-	-	Bal.	-	-	-
304 SS (measured)	7.95	18.41	1.32	0.59	-	-	71.73	-	-	-
IN 625 (ref.)	Bal.	20-23	0.5 max	0.5 max.	3-4	8-10	4	0.4	0.4	-
IN 625 (measured)	70.85	15.4$^{\Delta}$	-	-	-	8.49	4.82	-	0.44	-
NiCrAlY	67	22	-	-	-	-	-	-	10	1

(Δ: Cr, Mn and Fe may have energy peaks overlapping each other.)

4.2 Thermal Spray Equipment and NiCrAlY Coating Conditions

The Mettech Axial III™ System was used to melt and spray the powder onto the substrate materials. In contrast to a conventional plasma spray system injects powder through the radial powder port, the Mettech system utilizes a state-of-the-art axial powder injection system, in which powder is carried through the center powder port and ejects co-axially with the plasma gases. The main advantage of this system is the higher particle temperature and particle velocity, which enhances adhesion between the coating and substrate and produces denser coatings with reduced oxides as a result of more thermal and kinetic energy involved in the deposition process. Additionally, the full entrainment of the powder in the plasma jet will increase deposition efficiency.

Spray conditions are based on previous tests conducted at Carleton University [43], which provided excellent melt, low porosity and good adhesion. Several key process variables for atmospheric plasma spraying are powder size, current, flow rate and composition of working gas, spray distance and nozzle size [44]. The actual parameters used in this study are given in Table 4-3.

Table 4-3 Plasma spray parameters.

Powder size (μm)	Nozzle	Total flow rate (SL/min)	H_2 (%)	Current (A)	Distance (mm)	Powder feed rate	Carrier gas flow rate (SL/min)	Time (s)	Revolution of sample (rpm)
10-45	6/16	230	23	250	150	6	12	80	220

One of the coating samples was cut to examine the coating condition. The SEM cross-sectional image of the coating is illustrated in Figure 4-1. The NiCrAlY powder particles were all melted and well deposited onto the substrate.

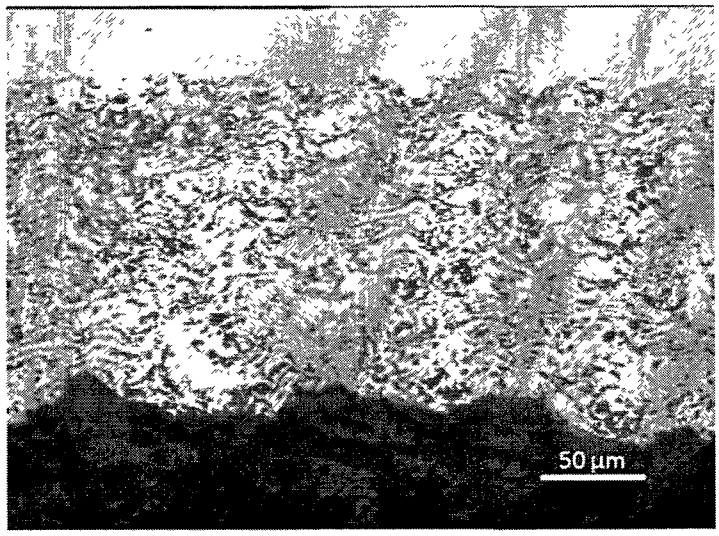

Figure 4-1 SEM cross-section image of NiCrAlY coating.

4.3 Surface Preparation Procedures

The effect of heat treatment was also included in this thesis. Previous research indicated post-coating heat treatment of MCrAlYs can promote the formation of γ/β two-phase structure in the MCrAlYs since only meta-stable γ phase is obtained in MCrAlYs due to high cooling rate during spraying [45]. Also, heat treatment will help lower the porosity and release the residual stresses within coatings in addition to the formation of alumina [46, 47, 48]. Therefore, the effect of heat treatment was evaluated for the bulk and NiCrAlY coated samples.

4.3.1 Button sample preparation

Each rod was cut into button samples of 3-5 mm in thickness. The samples were cut using a Buehler Isomet 1000 precision saw and then ground to 600 grit on a Buehler Handimet grinder. According to the test design, a second set of samples was ground and

polished to a mirror finish using 0.3 μm alumina paste. A third set of samples was vacuum heat-treated for 24 hours at 1050°C followed by furnace cooling. The fourth set was heat-treated in air for 24 hours at 1050°C followed by air cooling. Table 4-4 summarizes the surface processing details for each set of samples. Each set included samples with five different compositions. All samples were cleaned with alkaline solution in a Branson 2520 ultrasonic cleaner followed by methanol rinse and air drying.

Table 4-4 Surface preparation methods of button samples.

Sample set	Ground with 600 grit sand paper (G)	Polished to mirror finishing (P)	Vacuum heat treatment (VHT)	Air heat treatment (AHT)
1	√			
2	√	√		
3	√	√	√	
4	√	√		√

4.3.2 NiCrAlY coating samples

First set of the coated samples (IN 625) was polished by a Diamond Grinder and then ground to 600 grit using a Buehler Handimet grinder. The second set of the samples was further polished to a mirror finish using 1 μm alumina paste. A third set of samples was polished to a mirror finish and then heat-treated in air for 24 hours at 1050°C followed by air cooling. Furthermore, 304 SS coated with NiCrAlY (35 mm x 12 mm x 1.5mm) was also tested in the air heat-treated condition. Both substrate materials (IN 625 and 304 SS)

were included in the test. These substrate materials were cut to the size of 20 mm x 10 mm x 1.5mm and were ground and polished. Table 4-5 shows the details for each sample while Figure 4-2 displays specified areas within one sample. All NiCrAlY samples were cleaned, air dried and weighed immediately before being placed into the SCW autoclave.

Table 4-5 Samples condition of NiCrAlY coating test.

Samples ID	Description	Ground with 600 grit sand paper (G)	Polished to mirror finish (P)	Air heat-treated (AHT)
625-P	IN 625		√	
304-P	304 SS		√	
625-G	IN 625	√		
304-G	304 SS	√		
NiCrAlY/625-G	NiCrAlY on IN 625	√		
NiCrAlY/625-P	NiCrAlY on IN 625		√	
NiCrAlY/625-HT	NiCrAlY on IN 625		√	√
NiCrAlY/304-HT	NiCrAlY on 304 SS		√	√

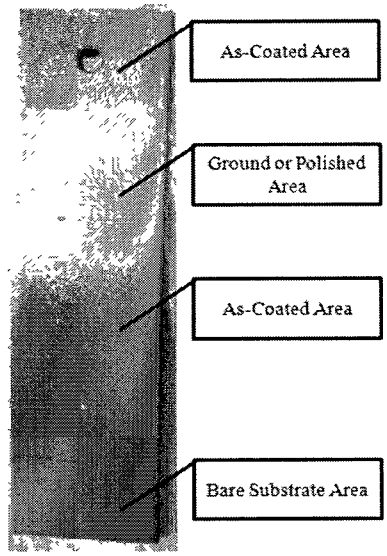

Figure 4-2 Specified areas of NiCrAlY sample.

4.4 Autoclave, Operating Procedures and Test Conditions

A SCW test system was developed in this study with the assistance of a summer co-op student. Additionally, machining and welding of jigs were carried out by machine shop staffs. During the initial stage of this study, numerous test runs were carried out to establish calibration curves. The main issues with the SCW system included: leakage, burst ring premature rupture, and inaccurate pressure control. It was a challenging task to setup the SCW system to reach the supercritical water condition. A great number of problems were overcome during this study. More details are given in the following sections.

4.4.1 Preparation of SCW Autoclaves Pressure Vessel (Reactors)

The autoclaves (reactors) used for this research are non-stirred pressure vessels from Parr Instrument Company. The reactors came with pressure cylinder, thermocouple, pressure

transducer, analog pressure gauge, safety burst disc, heating elements and controllers. A schematic diagram of the experimental apparatus is shown in Figure 4-3.All the reactor parts are labelled in Figure 4-4 and Figure 4-5. Many other systems had to be designed and assembled to get the reactors fully operational; these include: a chilling loop for the pressure transducer, safety enclosures to contain possible burst disc rupture, and a purge, pump and injection system to ensure only water was injected into the autoclave. Challenges such as repeated burst disc failures and persistent leaking problems had to be overcome before testing of coating samples.

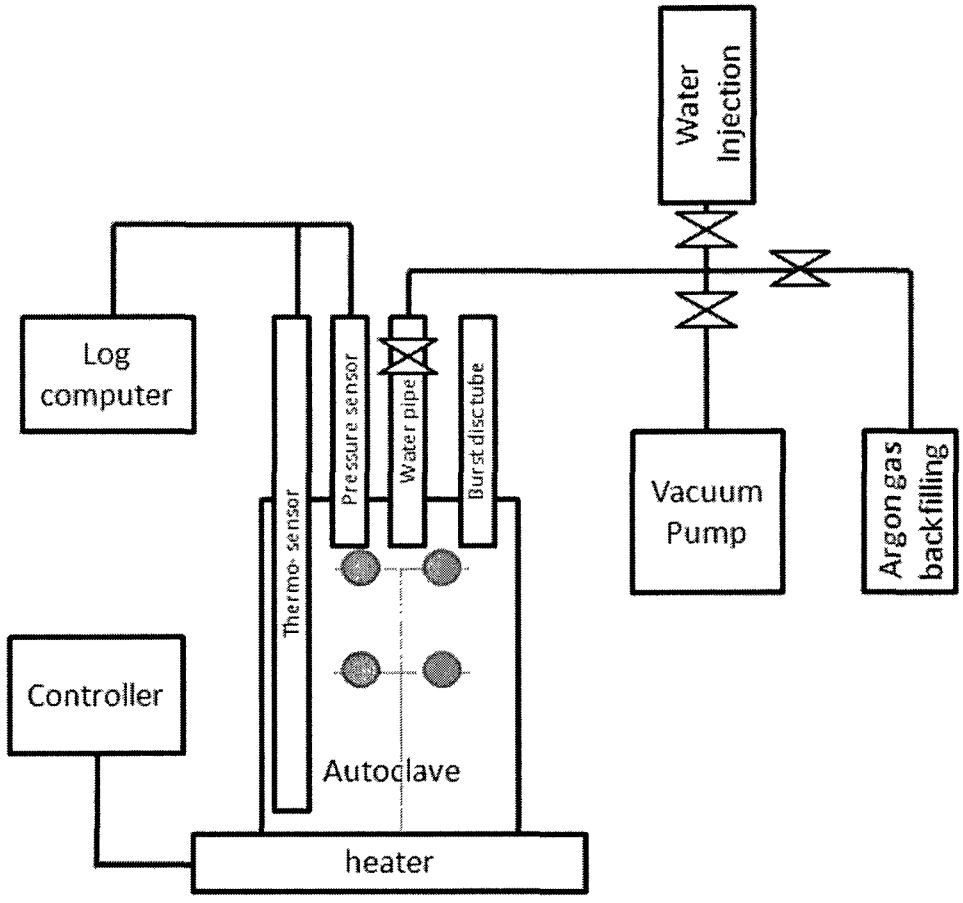

Figure 4-3 Schematic diagram of the SCW test system.

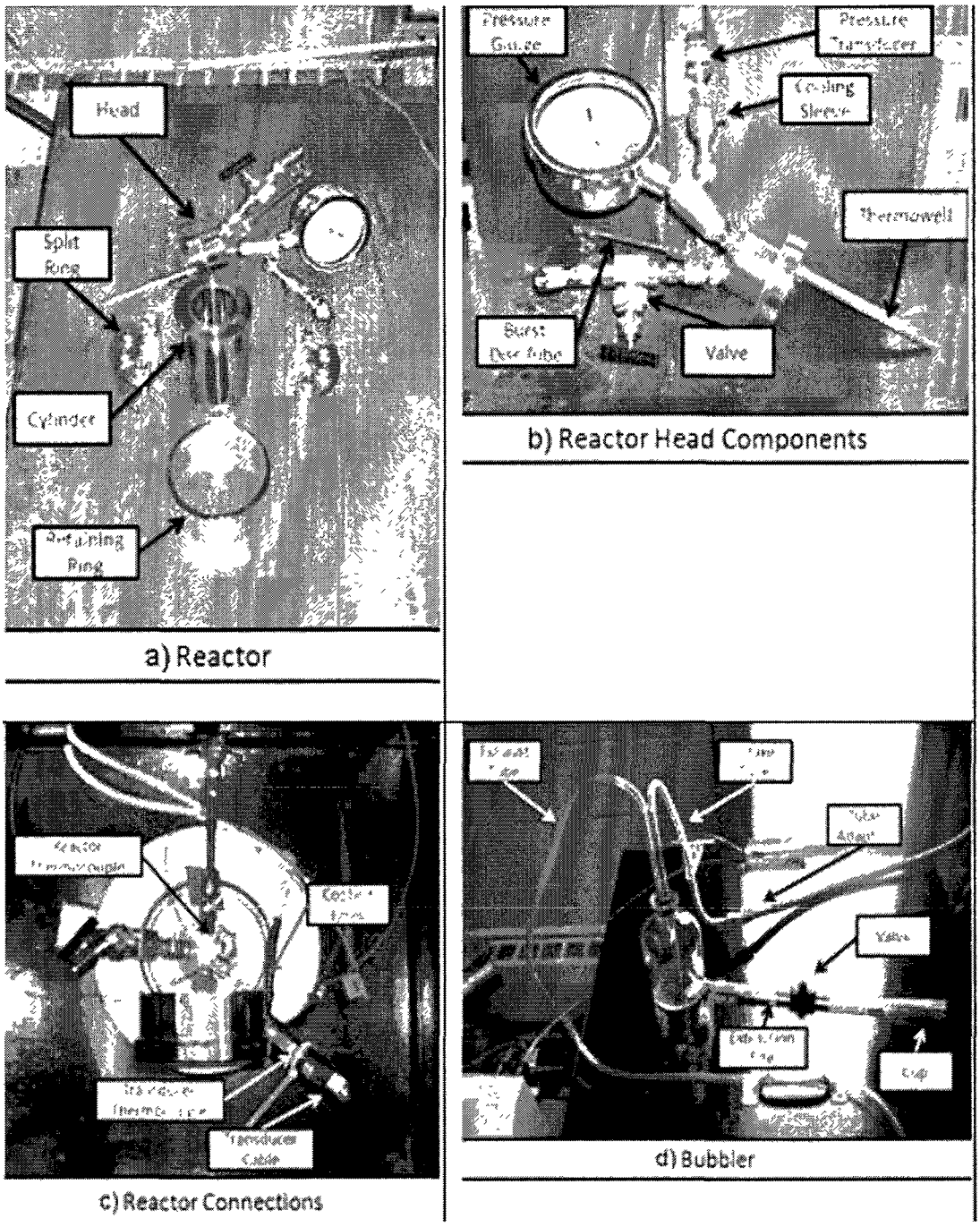

Figure 4-4 Naming of various reactor components

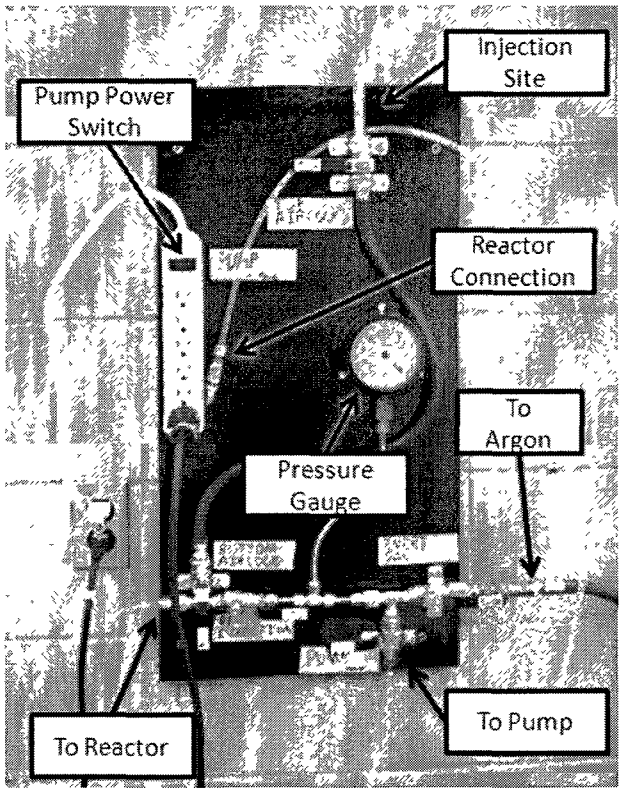

Figure 4-5 Purge, pump and injection system for filling the reactor with water while keeping impurities out.

4.4.1.1 Pressure Transducer

The maximum working temperature for the pressure transducers is 120°C. It has been observed that the output pressure value changes with transducer temperature. It is important to keep the pressure transducers at a low and stable temperature. To do this a Cole Parmer, Polystat chiller was connected to the cooling sleeve on the pressure transducer by Tygon tubing. A thermocouple attached to the pressure transducer showed that this chilling unit was effective, keeping the temperature of the transducer below 80°C at all running conditions.

4.4.1.2 Sample Holding Tree

In order to prevent galvanic corrosion, samples must be insulated from dissimilar metals during testing. The following "tree" was designed to hold the samples. The tree trunk was made of alumina. An alumina disc was used to insulate the reactor interior and the tree. The added benefits of this design are the lowered cost and the ability to place the alumina arms in any combination of the holes in the tree to accommodate various sizes of samples. The sample holding tree is shown in Figure 4-6.

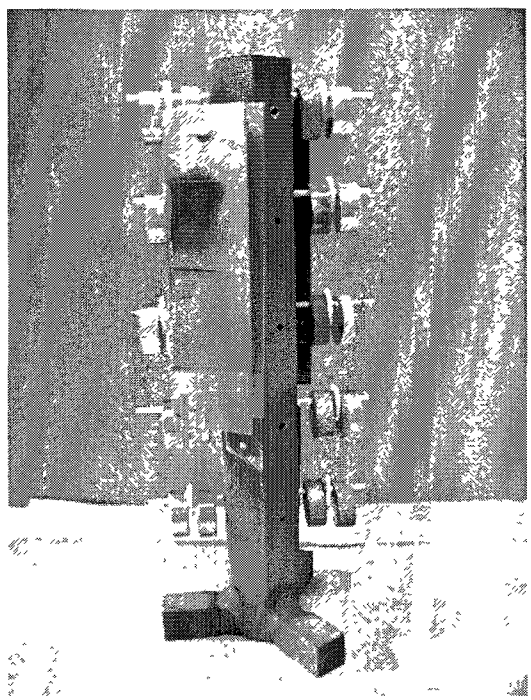

Figure 4-6 Sample holding tree with samples.

4.4.1.3 Safety Burst Discs and Enclosures

In order to provide a safeguard against a possible over pressurization, safety burst discs were fitted to the reactors. In addition to this passive safety measure, enclosures were constructed for the reactors. The enclosures were made of 1/8" mild steel panels welded to an angle iron frame. The enclosures are locked at all time when the reactors were pressurized.

4.4.1.4 Calibration Equations for Accurate Water Volume Injection

Since there is a temperature gradient within the reactor, the actual mean density of the water does not necessarily correspond to the measured temperature and pressure. In order to make sure the correct amount of water was added so as to meet the desired density, calibration equations were developed based on Equation (1).

$$V_a = \frac{(V_c - V_s) \times \rho_o}{\rho_w} + V_l \qquad \textbf{Equation (1)}$$

Where: V_a is the water to be added,

$V_c = 719$ ml and is the back calculated volume of the reactor,

V_s is the volume of the samples,

ρ_o is the density of the water at operational temperature and pressure,

$\rho_w = 998$ kg/m^3 and is the density of water added, and

$V_l = 7$ ml and is the correction factor for water lost in the piping.

A new calibration method, which takes a linear approximation of the water added vs. density achieved for all previous tests, has also been made. As shown in Figure 4-7, this

method was found to be much more accurate for higher and lower density tests. A new equation, developed based on the linear interpolation of test data, is given in Equation (2).

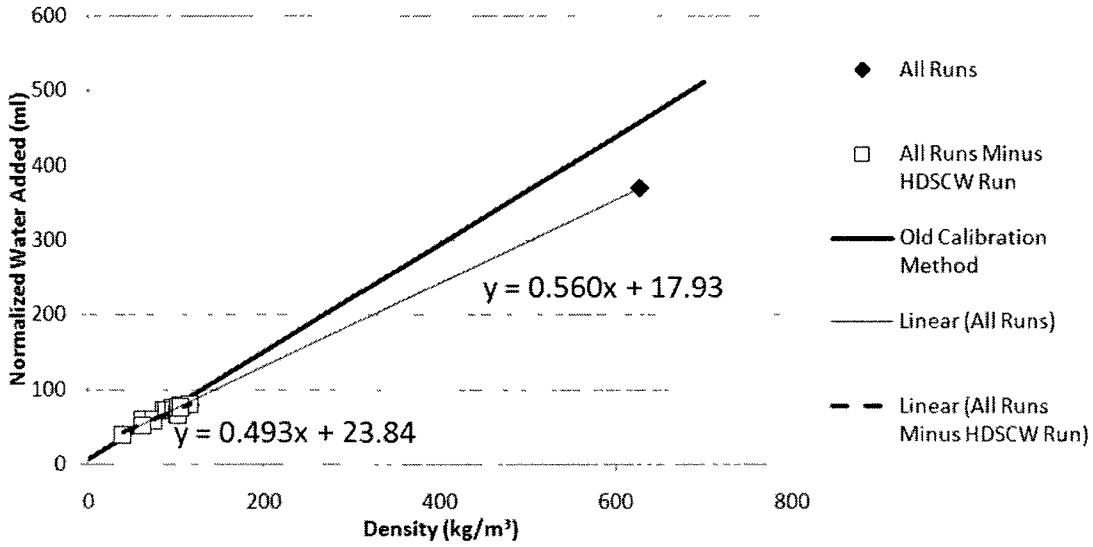

Figure 4-7 Water added (normalized volume) vs. density calculated from temperature and pressure readout.

$$V_a = (0.560 \times \rho_o + 17.9) \times \frac{V_c - V_s}{V_c} \qquad \textbf{Equation (2)}$$

Where: V_a is the water to be added,

The coefficients of 0.560 and 17.9 were obtained from the linear interpolation of Figure 4-7.

ρ_o is the density of the water at operational temperature and pressure,

$V_c = 525$ ml and is the true volume of the reactor, and

V_s is the total volume of the samples calculated based on weights and densities of the samples.

4.4.1.5 Creating and Injecting Water with Reduced Dissolved Oxygen

The effect of dissolved oxygen (DO) content in the water on sample's corrosion behaviour is very complex as described in Chapter 2, with high corrosion rates at either very high or very low dissolved oxygen [5]. It was determined to aim for low dissolved oxygen (<5 ppm) in this study since it simulates in-service conditions of SCW closely. Water with low DO is produced by boiling the water while simultaneous bubbling with nitrogen for at least 30 min. While low DO values are possible with this procedure, the repeatability is low as the DO values range from 0.2 to 0.9 ppm. It was challenging to design a system to inject low DO water, since the water must not come into contact with air as the oxygen dissolves into the water rapidly. A system involving purging, pumping and water injection was designed for this work. The details of this system are shown in Figure 4-5. The autoclaves were first pumped with a mechanical pump three times and purged with argon gas twice. After the third pump, the water is injected through a silicone tube with a syringe.

4.4.1.6 Autoclave Leakages

During all test runs, pressure reduced over time indicating leakages in the system. After many trials, the main source of the leakage was found to be from the thermowell where a large temperature drop was observed due to steam formation within the thermowell. This observation was confirmed by pressurizing the reactor's ambient temperature to 200 psi and coating the reactor in a SNOOP leak detection solution. The thermowell leakage was solved by changing the thermowell gasket from silver to grafoil, and increasing the torque on the thermowell from 40 to 50 ft-lb. After a complete overhaul of the reactors

and tightening all fittings to specifications, a secondary leakage remained. The secondary leak was traced to the main pressure vessel seal. The torque on the main seal bolts was increased from 50 to 60ft-lb to the bolts which resolved the leakage issue.

4.4.1.7 Silicon Contamination

It has been found that silicone based grease on the main head gasket will improve the sealing characteristics of the gasket; however, this grease has been found to contaminate the water. The silicone dissolves into the water at test temperature and deposits a Si-containing substance on the samples during autoclave cooling cycle. An alternative way of sealing the main gasket has yet to be found.

4.4.2 SCW Test of Button Samples

The samples were hung from the alumina arms of the "tree" placed on a ceramic disc in the autoclave in order to prevent contact with the wall. Also, alumina spacers were placed between the specimens to prevent the samples from contacting each other. A vacuum was created in the vessel and a calculated amount of water was injected into the vessel to achieve pre-determined pressure at the test temperature. The dissolved oxygen concentration in the water was controlled by distillation first and nitrogen gas bubbling subsequently for over 30 minutes. The final dissolved oxygen content was measured before each test run. A self-filling ampoule (CHEMets Kit, K-7501, USA) was used for the measurement of DO through colorimetric analysis. The pH value was measured by non-bleeding pH-indicator strip (ColorpHast, pH 0-14, Germany). After SCW corrosion

test, another water sample was taken for DO and pH measurements. A slight decrease in pH was observed after testing indicating acidity increased.

Table 4-6 provides a summary of the test conditions. Due to the leakage of the autoclave, the pressure decreased slightly during stage 1. For stage 2, it decreased somewhat faster. Conditions were kept within the supercritical region by raising the temperature from 495 to 540°C. Another 500 hours was planned for stage 2 of the test, however, only 440 hours was made due to the leakage. The plots of temperature and pressure as a function of time are shown in Figure 4-8 and Figure 4-9.

Table 4-6 Test parameters (run of button samples).

Test Stage	Temp. (°C)	Pressure (start/end) (MPa)	Time (hr)	DO level (start/end) (ppm)	pH value (start/end)	Density (start/end) (Kg/m^3)
Stage 1	500	27.58/25.92	500	1.0/6	6/5	102.4/94.17
Stage 2	495-540	27.58/22.41	440	0.6/6	6/5	104.2/70.45

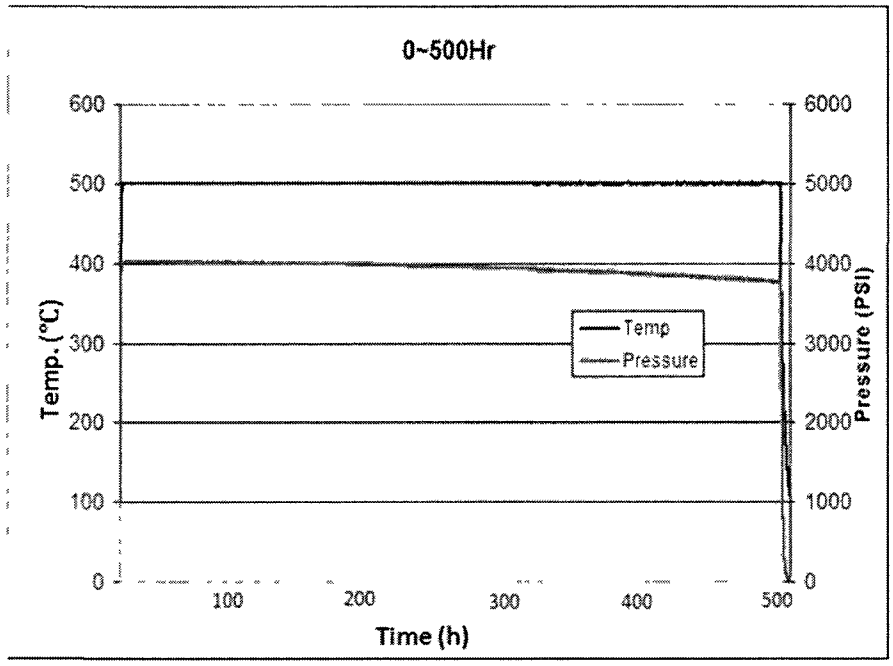

Figure 4-8 Pressure and temperature vs. time for stage 1 of testing button samples.

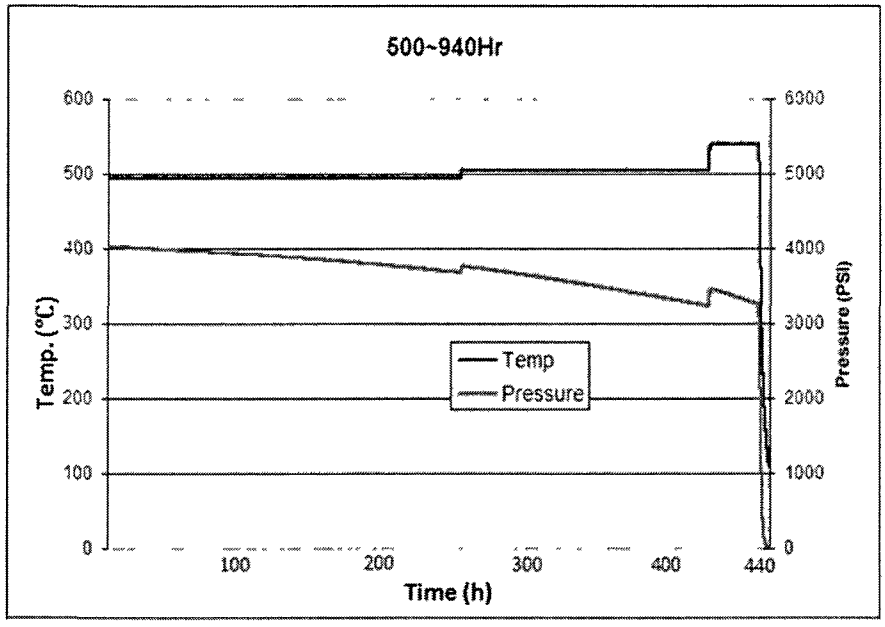

Figure 4-9 Pressure and temperature vs. time for stage 2 of testing button sample.

4.4.3 SCW Tests of NiCrAlY Coating Samples

In order to simulate the test conditions similar to that of the button samples, the temperature and pressure were set as close as possible to the previous runs. The plots of temperature and pressure in stage 1 and 2 with respect to time are shown in Figure 4-10 and Figure 4-11, respectively. With the improvements to the setup procedure describe earlier, the leakage in autoclave was less than the first two runs. Table 4-7 provides a summary of the test conditions.

Table 4-7 Test parameters (run of NiCrAlY coating samples).

Test Stage	Temp. (°C)	Pressure (start/end) (MPa)	Time (hrs)	DO level (start/end) (ppm)	pH value (start/end)	Density (start/end) (Kg/m^3)
Stage 1	500	27.10/25.58	500	1.0/6	6/5	99.94/92.5
Stage 2	495-540	27.13/26.23	440	0.6/6	6/5	101.9/85.32

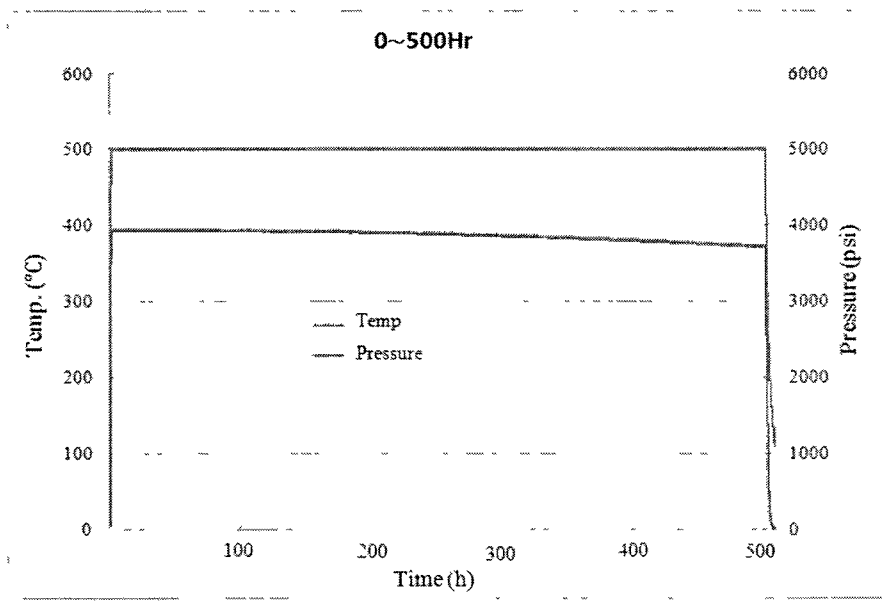

Figure 4-10 Pressure and temperature vs. time for stage 1 of testing NiCrAlY coated samples.

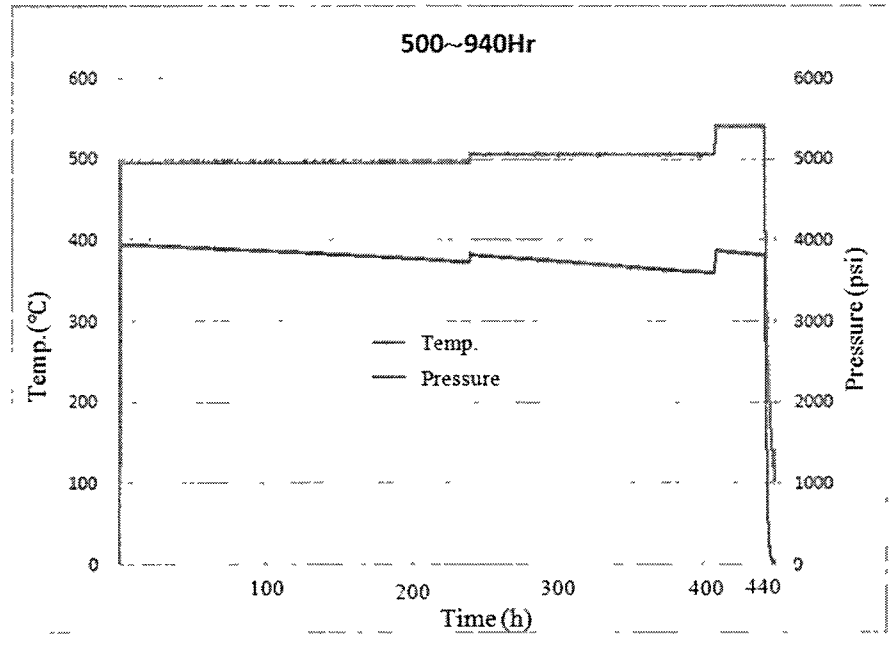

Figure 4-11 Pressure and temperature vs. time for stage 2 of testing NiCrAlY coated samples.

4.5 Weight Change Measurement and Normalization

Sample weights before and after each test were measured twice using an analytical scale (Mettler-Toledo, AG285, USA) in order to minimize the error of operation. After each stage was completed, the samples were taken out and first cleaned by methanol before being weighed. To standardize the weight change amount, a unit of $mg/dm^2/day$ was introduced.

4.6 SEM

The analysis of surface morphology and elemental distribution of samples after tesing was investigated using scanning electron microscope (SEM) and energy-dispersive X-ray spectroscopy (EDS) technique. The samples were ultrasonically cleaned before being loaded into the vacuum chamber of the SEM. EDS analysis was used to qualitatively determine the compositions of the samples before and after SCW testing. The SEM used in this study is a Tescan Vega II XMU VPSEM, in conjunction with an Oxford EDES Instruments (Oxford Inca Energy 250X). An image of this facility at Carleton University is shown in Figure 4-12.

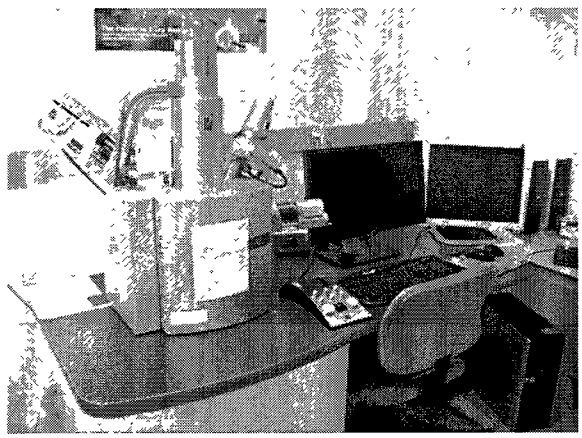

Figure 4-12 Image of SEM facility in Carleton University.

5. Results and Discussion

The subsequent sections will detail the test results of the bulk (button samples) and NiCrAlY coating samples after being exposed to SCW for 940 hours.

5.1 Visual Appearance of Button Samples after SCW Testing

Upon removing the samples from the autoclave after the first and second stage of the SCW testing, their surface appearances were recorded as shown in Figure 5-1 and Figure 5-2. The surface scales varied with composition and surface preparation. Samples without any heat treatment, G (Ground) and P (Polished), appeared quite smooth and some displayed a metallic shine. The vacuum heat-treated samples exhibited darker surface features than the polished and ground samples. Several air furnace heat treated samples (Ni20Cr and Ni5Al) showed heavy scale and scale spalling. The surface conditions did not change significantly after 940 h testing when compared with that after the 500 h test.

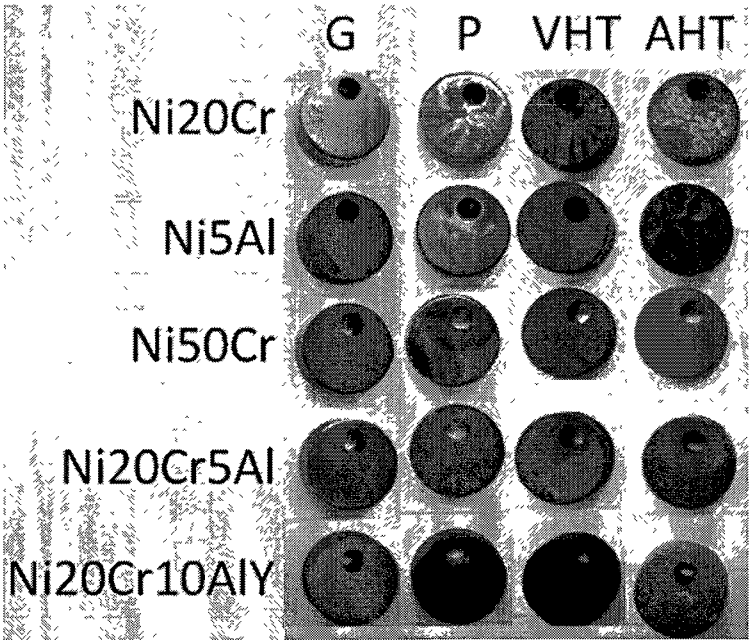

Figure 5-1 Sample surface conditions after Stage 1 (500h)-run of button.

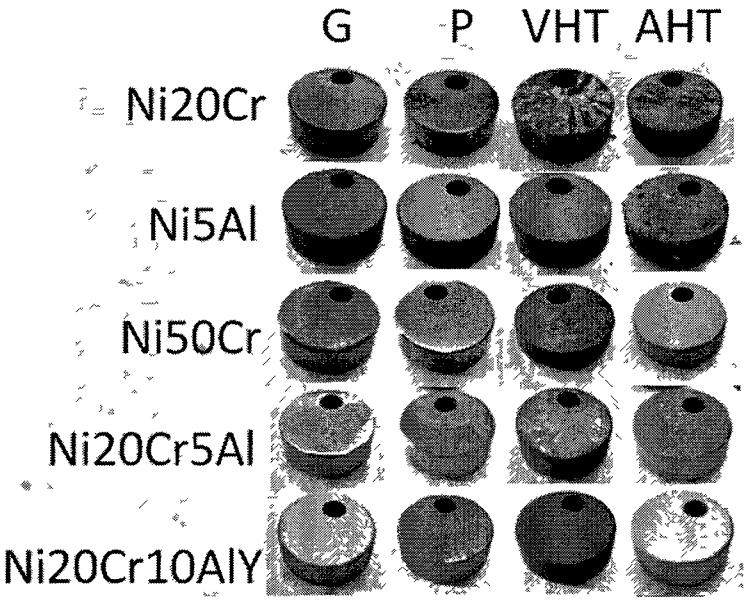

Figure 5-2 Sample surface conditions after Stage 2 (940h)-run of button.

5.2 Weight Change for Button Samples after SCW Testing

Sample weight changes after testing are shown in three figures, representing the results after the first stage of testing (500h) (Figure 5-3), second stage of the testing (440h) (Figure 5-4), and finally the cumulative 940h (Figure 5-5). Overall, the samples that had been ground and polished showed the least weight gain, while some of the air heat-treated samples showed a significant weight loss after 500 h exposure to SCW. Scale spalling was believed to be the cause for the weight loss in some of the air heat treated samples (Ni20Cr, Ni50Cr and Ni20Cr10AlY). Small blackish particles were found in the water after each stage of the test. Vacuum heat treatment seemed to have caused more weight gain during the first 500-hour exposure to SCW than stage 2 of the test. Ni20Cr5Al exhibited the lowest and most consistent weight change compared to the other samples. This was also the one of the air heat-treated samples that did not experience

weight loss or heavy scale formation after both stages of testing.

During the stage 2 of the test, the weight changes seemed to have stabilized and all samples displayed a slight weight gain except for the air heat-treated Ni5Al sample, which experienced scale spalling during stage 2. Samples that have been ground with 600 grit sand paper showed the least weight change.

The cumulative weight change after a total of 940 h exposure to SCW showed a similar trend to that observed after the first 500 h, i.e., grinding and polishing resulted in lower and stable weight gain for all sample compositions while air furnace heat-treatment caused weight loss to samples Ni20Cr, Ni5Al and Ni50Cr due to the spalling of surface scale. Vacuum furnace heat-treatment resulted in steady surface film formation for all sample compositions. The surface morphology of various samples is further discussed in the next section.

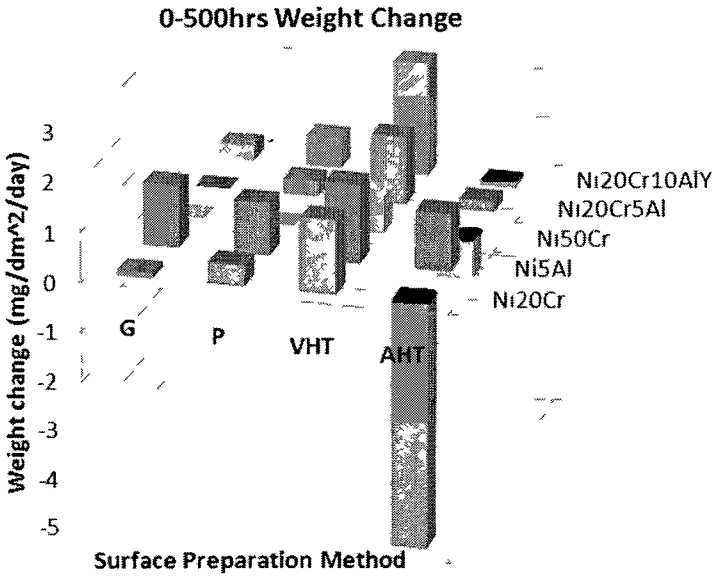

Figure 5-3 3-D bar chart showing the weight change (Z-Axis) as a function of surface preparation (X-Axis) and sample type (Y-Axis) during Stage 1 of testing.

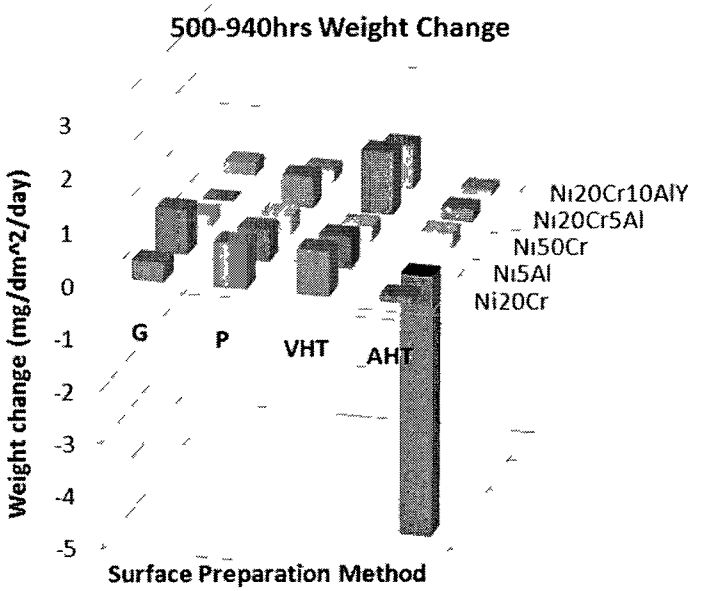

Figure 5-4 3-D bar chart showing the weight change (Z-Axis) as a function of surface preparation (X-Axis) and sample type (Y-Axis) during Stage 2 of testing.

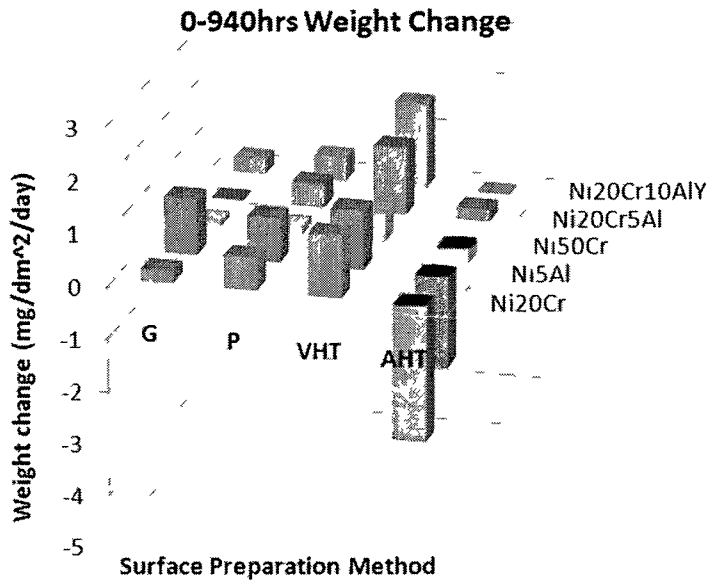

Figure 5-5 3-D bar chart showing the cumulative weight change (Z-Axis) as a function of surface preparation (X-Axis) and sample type (Y-Axis).

5.3 SEM Analysis Results of Button Samples

The sample microstructure and surface morphology after 940 hours of testing was characterized using SEM along with chemical composition analysis using the SEM-EDS technique.

5.3.1 Samples before SCW Test

Button samples in the as-received condition were polished and etched in order to examine the grain size and phase features of each composition. The metallographic samples were etched using Marble's reagent, which contains 50ml 50% hydrochloric acid (HCl), 50ml distilled water, 10g copper sulfate ($CuSO_4$) and a few drops of sulfuric acid (H_2SO_4). After etching, the samples were examined using SEM. As can be seen in Figure 5-6,

nickel, chromium and aluminum were distributed evenly in the alloys of Ni20Cr and Ni5Al, although the grain boundaries of sample Ni5Al were more regular than that of Ni20Cr. As for sample Ni50Cr with elevated chromium content, two phases were found and this is consistent with the Nickel-Chromium phase diagram. More pores were observed in Ni20Cr5Al and Ni20Cr10AlY. The large pores detected in Ni20Cr10AlY could have led to more surface exposure to SCW during testing and resulted in poorer corrosion performance. The X-ray mapping results of each element in five alloys are presented in Figure 5-7. Both Ni50Cr and Ni20Cr10AlY showed segregated Cr distribution and Ni20Cr10AlY also contained Al rich islands.

The surfaces of vacuum and air heat-treated samples were also analyzed before exposure to SCW. The heat treatments prior to SCW exposure were intended to promote the formation of a thin oxide film. The type of the oxide formed depends upon the sample composition. The EDS results showed that alumina was formed on vacuum heat-treated Ni20Cr5Al and Ni20Cr10AlY (Table 5-1) while chromia formation was observed on the air heat-treated Ni20Cr and Ni50Cr samples. Noticeably, a large amount of alumina was formed in Ni20Cr10AlY during air heat treatment as highlighted in Table 5-1 (two rows of EDS results are included in the table, one includes oxygen and one excludes oxygen).

The sample surface morphologies after vacuum heat treatment are shown in Figure 5-8. While the Ni20Cr and Ni5Al samples exhibited very smooth and light surface features, the oxides formed on samples of Ni50Cr and Ni20Cr5Al are quite porous. For Ni20Cr10AlY sample, the oxides are chromia and alumina in nature.

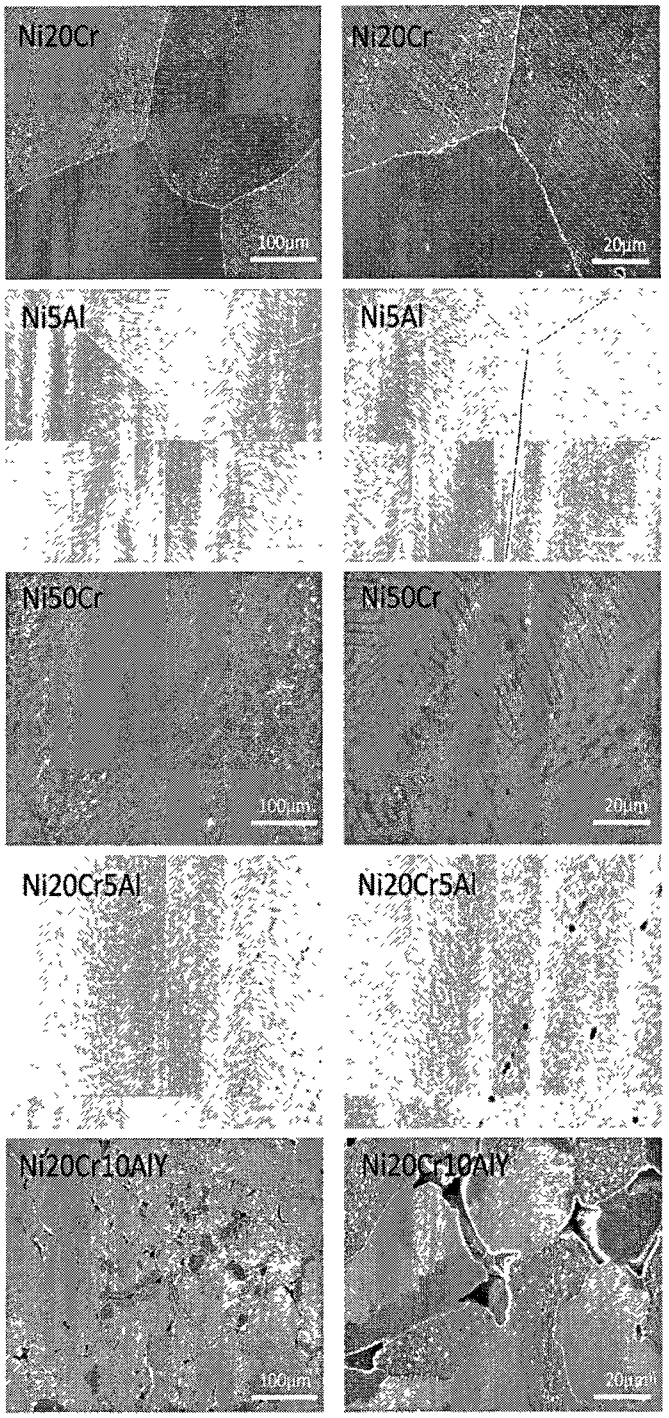

Figure 5-6 SEM images (Left: Low Mag., Right: High Mag.) of five etched samples in the bulk condition before testing.

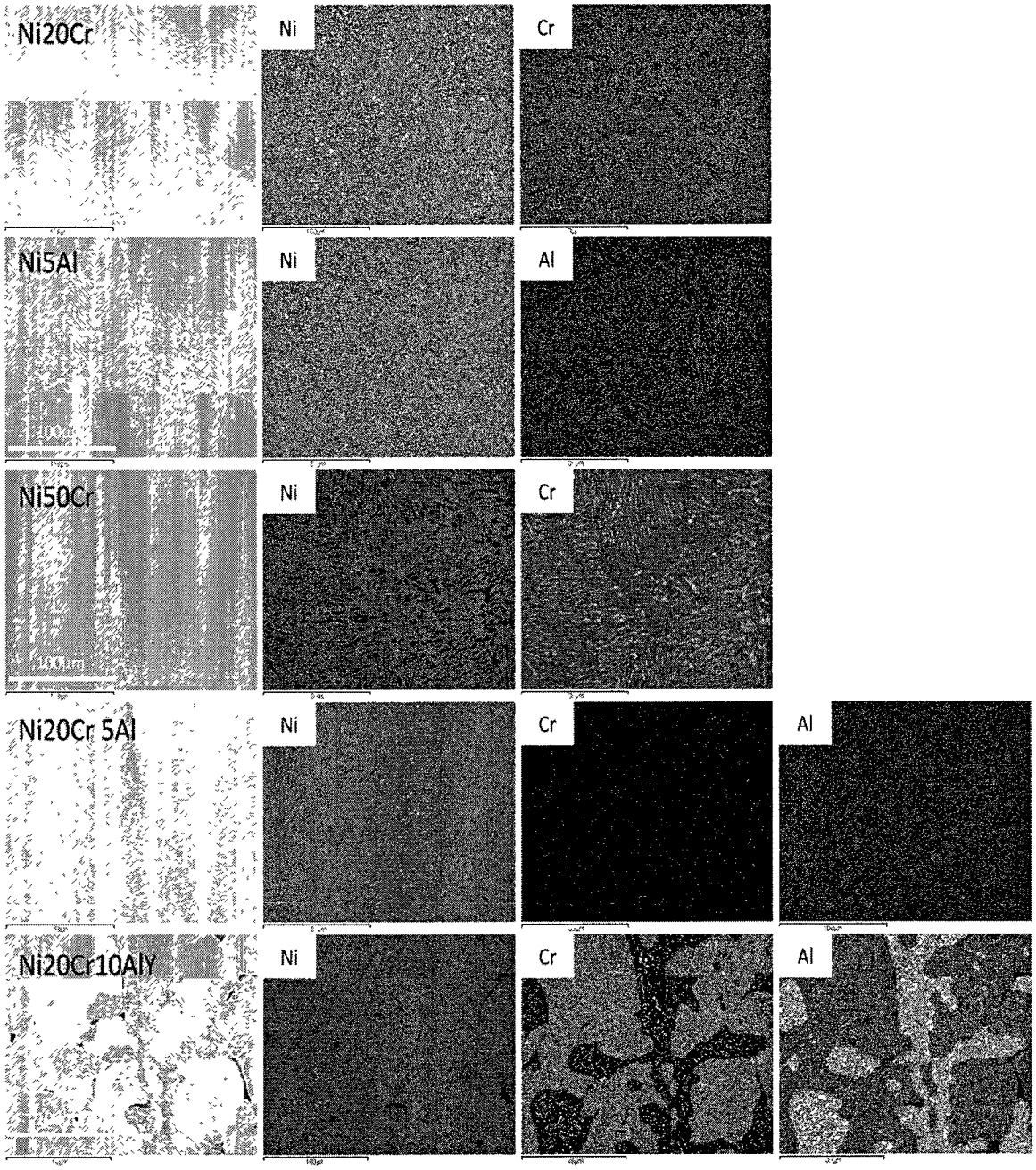

Figure 5-7 Mapping results of five etched samples in the bulk condition before testing

The air furnace heat-treated samples had different surface morphologies than the vacuum heat-treated samples. The Ni20Cr sample was covered with a thick oxide layer (Figure 5-9) with angular morphology, suggesting more oxide growth under this condition. The Ni5Al sample showed no evidence of a surface oxide, and some localized surface pitting was observed. Scale flaking was observed for the Ni50Cr and Ni20Cr10Al samples, although oxide films formed under the scale. For the Ni20Cr10AlY sample, dense oxides also formed under the upper flaky layer. The surface compositions after air furnace heat-treatment are summarized in Table 5-1 as well. (Δ: Cross contamination from other samples during SCW test)

Table 5-1 EDS surface analysis results for samples after VHT and AHT (wt%).

		Al	Cr	Ni	O	Y
Ni20Cr	Nominal composition	-	20	80	-	-
	Vacuum H/T	-	16.9	83.1	-	-
		-	16.9	83.1	0*	-
	Air Furnace H/T	-	14.95	58.95	26.1	-
		-	20.23	79.77	0*	-
Ni5Al	Nominal composition	5	-	95	-	-
	Vacuum H/T	4.52	2.71$^{\Delta}$	92.77	-	-
		4.52	2.71$^{\Delta}$	92.77	0*	-
	Air Furnace H/T	5.88	-	85.3	8.82	-
		6.45	-	93.55	0*	-
Ni50Cr	Nominal composition	-	50	50	-	-
	Vacuum H/T	-	37	60.56	2.44	-
		-	37.93	62.07	0*	-
	Air Furnace H/T	-	63.78	-	36.22	-
		-	100	-	0*	-
Ni20Cr5Al	Nominal composition	5	20	75	-	-
	Vacuum H/T	11.27	6.55	76.88	5.29	-
		11.9	6.92	81.18	0*	-
	Air Furnace H/T	8.84	29.39	42.26	19.51	-
		10.98	36.51	52.51	0*	-
Ni20Cr10AlY	Nominal composition	10	20	69	-	1
	Vacuum H/T	14.49	4.72	73.28	5.19	2.32
		15.28	4.98	77.29	0*	2.45
	Air Furnace H/T	24.53	14.32	25.80	35.35	-
		37.94	22.15	39.91	0*	-

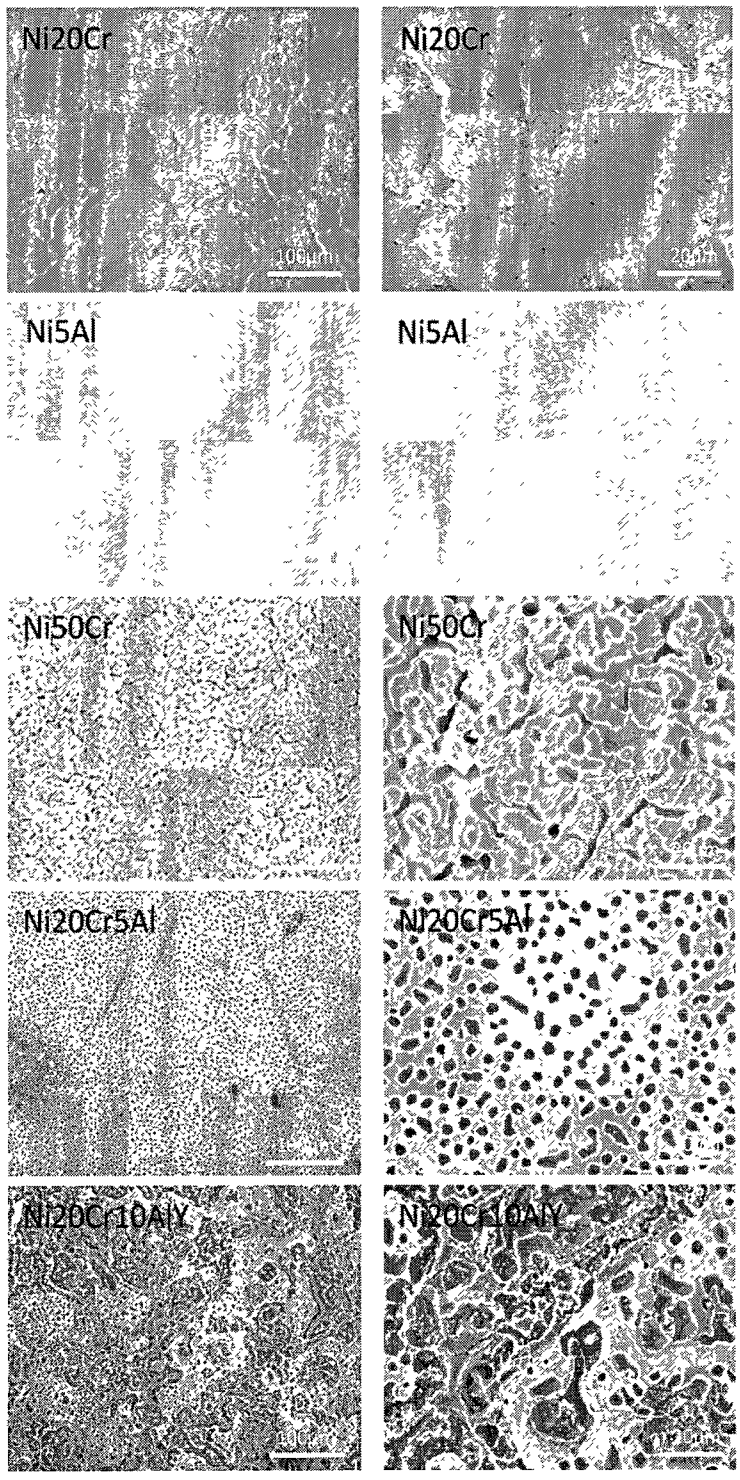

Figure 5-8 SEM Images (Left: Low Mag., Right: High Mag.) of Samples in the Vacuum-Heat Treated Condition (VHT).

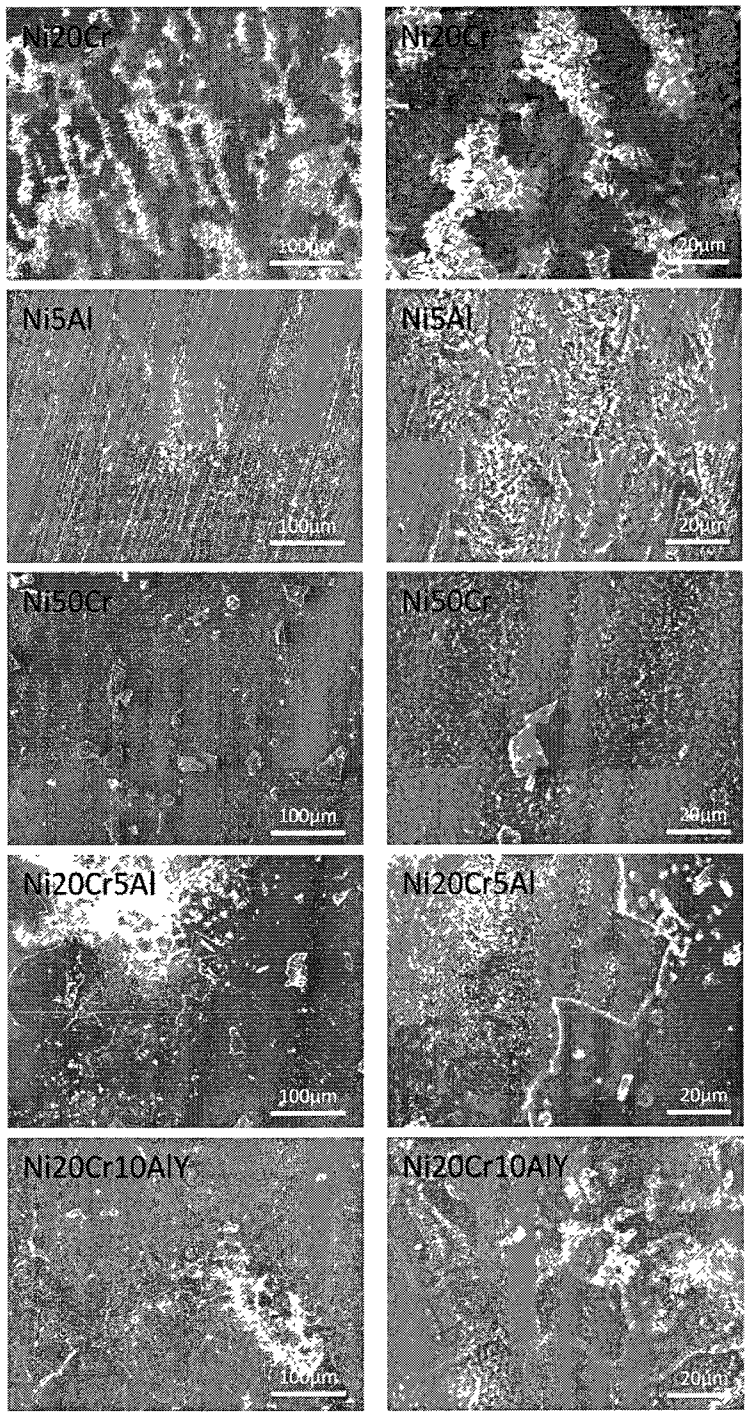

Figure 5-9 SEM images (Left: Low Mag., Right: High Mag.) of samples in the air-heat treated condition (AHT).

5.3.2 Samples after SCW Exposure

Samples after both stages of testing were analyzed by SEM/EDS. The results are presented in the following sections.

5.3.2.1 Ni20Cr

The surface features of the Ni20Cr sample after SCW testing showed that both ground and polished surfaces still maintained the original surface preparation features, i.e., polishing lines (Figure 5-10). The images also showed the deposition of spherical Si-rich contaminants from the use of silicon sealant in the system. The Cr content was higher than the nominal composition in the ground sample (Table 5-2, where * indicates oxygen being excluded in EDS results) suggesting further chromia formation and possibly Cr diffusion to the surface due to cold working (from grinding). The vacuum heat-treated sample continued to develop a surface film within the grains and along the grain boundaries, while the air heat-treated sample displayed surface scale delamination. The surface film formed on vacuum heat-treated samples after SCW exposure is believed to contain Cr-rich and Ni-rich oxides based on the chemical composition given in Table 5-2. Cr depletion was found on the air heat-treated sample suggesting spallation of the Cr-rich oxide may have occurred during SCW test. Since all samples were found to have been contaminated by a Si-rich material, Si was excluded from the EDS analysis in order to properly quantify the concentrations of oxygen and metallic elements. The findings from the SEM analysis were consistent with the weight change results given in Figure 5-5, where the air heat-treated Ni20Cr showed a weight loss, while the polished and ground samples exhibited small weight gains.

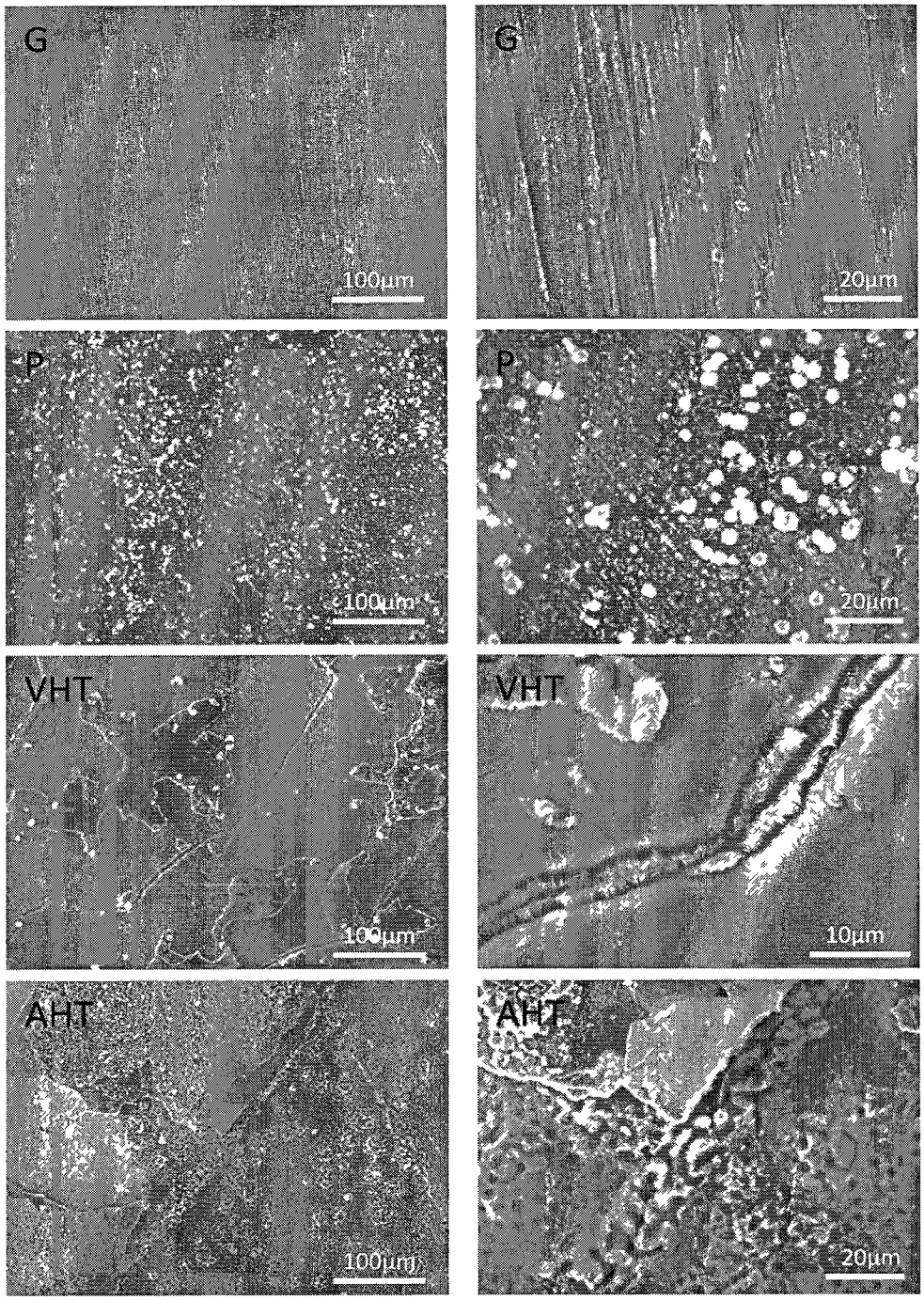

Figure 5-10 SEM images (Left: Low Mag., Right: High Mag.) of Ni20Cr samples after 940 h SCW exposure

Table 5-2 EDS surface analysis results for Ni20Cr sample after 940h SCW exposure (wt%)

Ni20Cr	Cr	Ni	O
Ground	25.57	53.44	20.99
	32.36	67.64	0*
Polished	7.93	52.69	39.38
	13.08	86.92	0*
Vacuum H/T	18.05	67.9	14.05
	21	79	0*
Air Furnace H/T	6.01	68.39	25.6
	8.08	91.92	0*

5.3.2.2 Ni5Al

The surface preparation methods also significantly influenced the surface morphology of the Ni5Al samples. Grinding and polishing resulted in comparable surface features (scratch lines) before and after testing while vacuum heat-treatment revealed island-like phase formation. In particular, air furnace heat-treatment generated heavy surface scale which began to delaminate upon exposure to SCW, causing weight loss. EDS analysis results (Table 5-3) confirmed oxide formation on the surface. The Al content was slightly elevated for the air heat-treated sample, suggesting more alumina formation as a result of heat treatment. Other samples showed similar Al and Ni contents as the nominal composition when oxygen was excluded in the EDS analysis (indicated by * in the table).

Table 5-3 EDS surface analysis results for Ni5Al sample after 940h SCW exposure (wt%)

Ni5Al	Al	Ni	O
Ground	4.14	69.33	26.53
	5.63	94.37	0*
Polished	3.05	73.86	23.09
	3.97	96.03	0*
Vacuum H/T	3.57	79.71	16.72
	4.29	95.71	0*
Air Furnace H/T	5.32	57.2	37.48
	8.51	91.49	0*

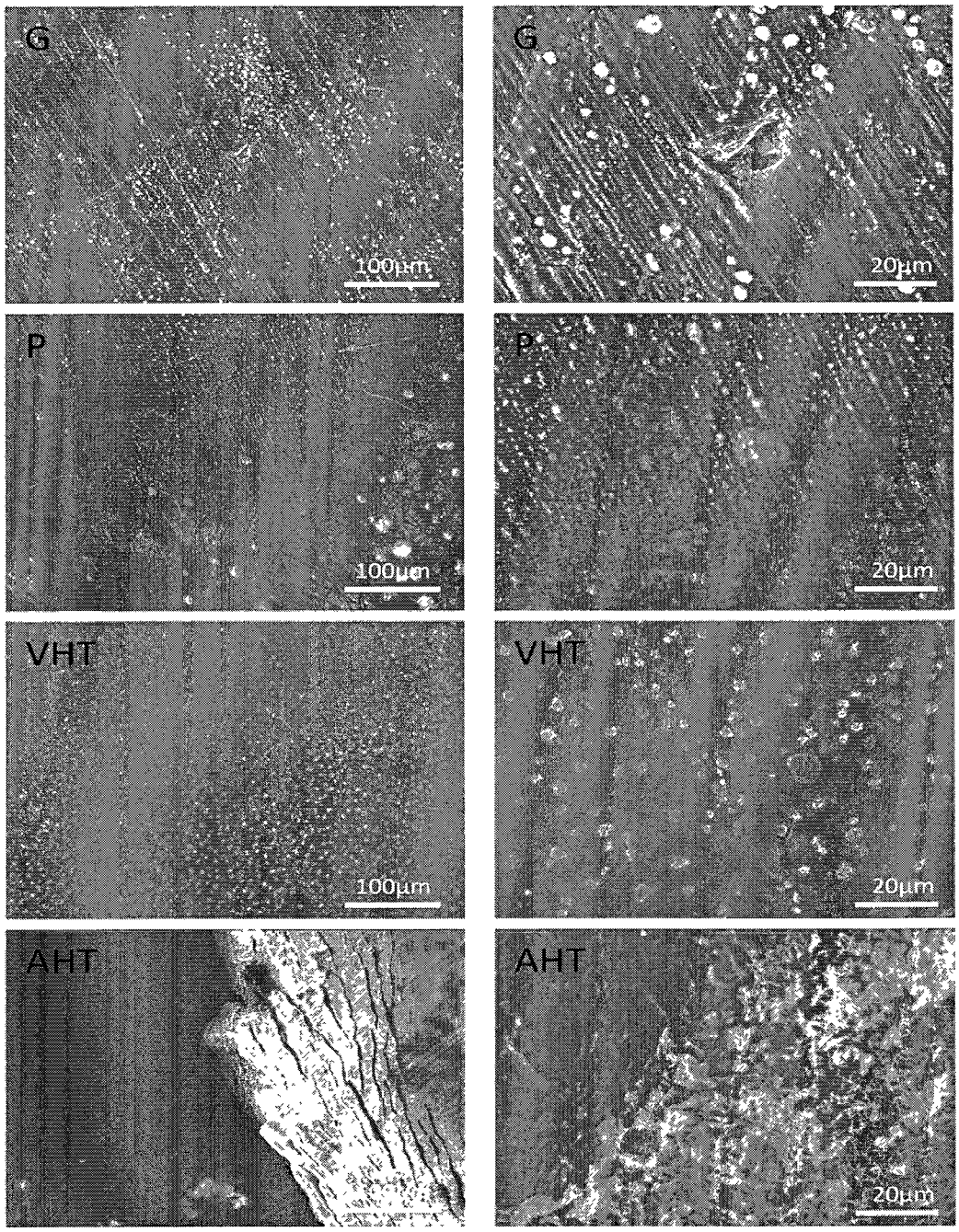

Figure 5-11 SEM Images (Left: Low Mag., Right: High Mag.) of Ni5Al Samples after 940 h SCW Exposure.

5.3.2.3 Ni50Cr

For the Ni50Cr samples, the surface morphology changed somewhat from that of Ni20Cr (Figure 5-10), as shown in Figure 5-12. The ground surface was largely intact with visible scratch lines from grinding, while small surface depressions were observed on the polished surface. Elevated Cr content compared to the nominal composition was detected on the ground surface after 940 h SCW testing. The vacuum heat-treated sample showed the formation of a porous surface phase, and from the EDS results, given in Table 5-4 , it is likely to be Ni-rich oxide (NiO). The most noticeable changes were the complete lack of scale loss in the as-heat-treated Ni50Cr sample (Figure 5-12) and the presence of a discrete phase on the surface. Since Ni was not detected on the surface (Table 5-4), these discrete particles are believed to be Cr_2O_3. The weight loss for the air heat-treated Ni50Cr sample was moderate, indicating the more adherent nature of the chromium oxide formed compared to the film that formed on the low Cr sample (Ni20Cr).

Table 5-4 EDS surface analysis results for Ni50Cr sample after 940h SCW exposure (wt%).

Ni50Cr	Cr	Ni	O
Ground	43.42	28.32	28.26
	60.52	39.48	0*
Polished	43.07	40.37	16.56
	51.62	48.38	0*
Vacuum H/T	19.42	45.65	34.93
	29.84	70.16	0*
Air Furnace H/T	63.63	-	36.37
	100	-	0*

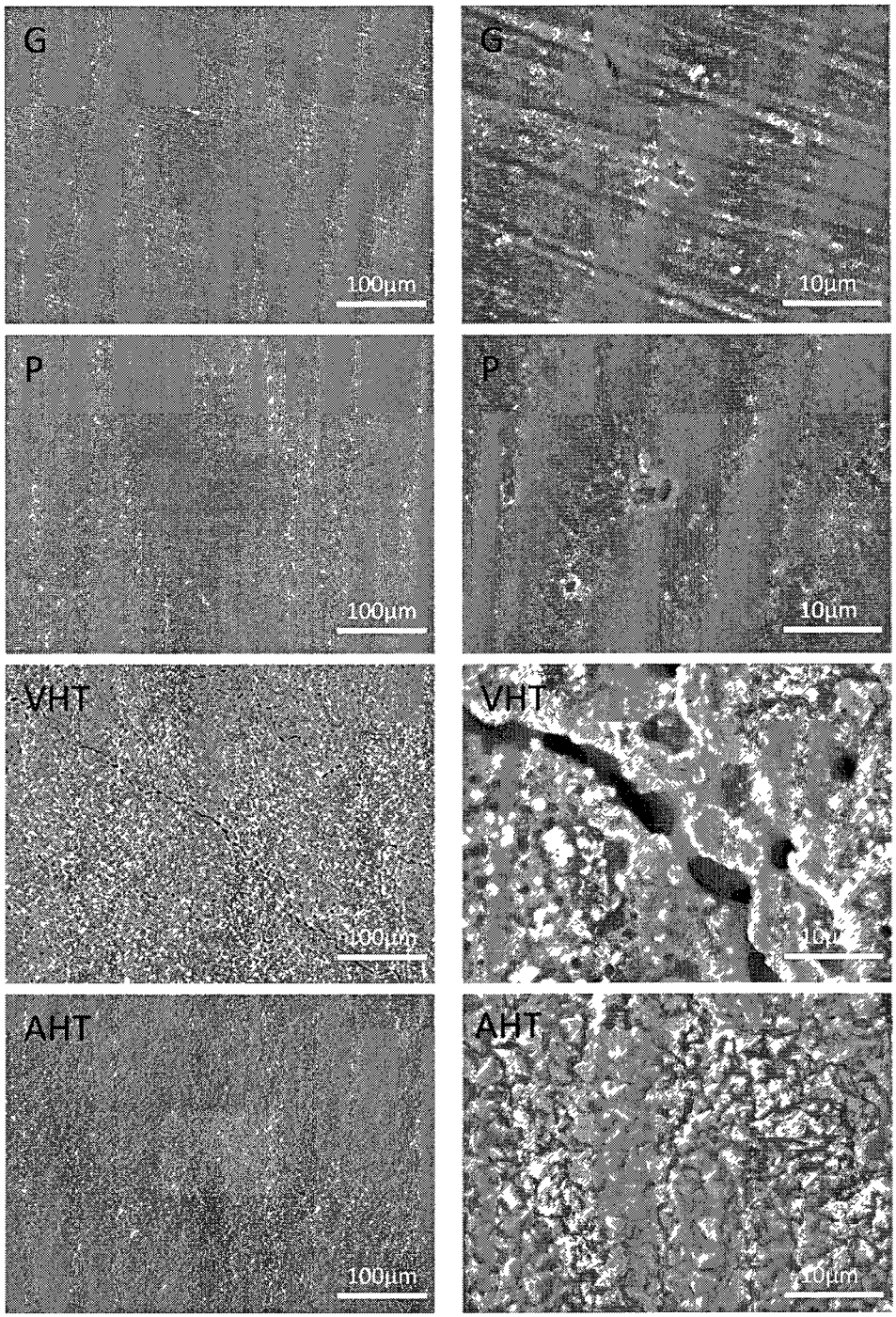

Figure 5-12 SEM images (Left: Low Mag., Right: High Mag.) of Ni50Cr samples after 940 h SCW exposure.

5.3.2.4 Ni20Cr5Al

The Ni20Cr5Al samples exhibited the best corrosion resistance among the bulk alloys tested. The ground sample showed very little difference compared to the sample before SCW testing; only polishing lines are visible, as shown in Figure 5-13. The EDS results (Table 5-5) also confirmed minor changes in the surface composition. It is apparent that this alloy composition would be a good choice for further testing in a SCW reactor (for an extended period of time). The polished sample showed a slightly uneven surface after SCW testing, however, no obvious pitting was observed. The vacuum and air furnace heat-treated samples seemed to have formed a protected layer enriched in Al and Cr/Al, respectively. Since vacuum heat treatment is known to promote Al_2O_3 formation, it is believed that a thin Al_2O_3 layer formed on the surface prior to the SCW test. Air furnace heat treatment encouraged both Cr_2O_3 and Al_2O_3 formation as shown by the elevated Cr and Al content on the surface (Table 5-5).

Table 5-5 EDS surface analysis results for Ni20Cr5Al sample after 940h SCW exposure (wt%).

Ni20Cr5Al	Cr	Al	Ni	O
Ground	19.35	3.83	68.15	8.67
	21.19	4.19	74.62	0*
Polished	8.84	1.22	51.85	38.09
	14.28	1.97	83.75	0*
Vacuum H/T	3.23	6.44	68.18	22.15
	4.15	8.27	87.58	0*
Air Furnace H/T	28.63	5.36	36.18	29.83
	40.8	7.64	51.56	0*

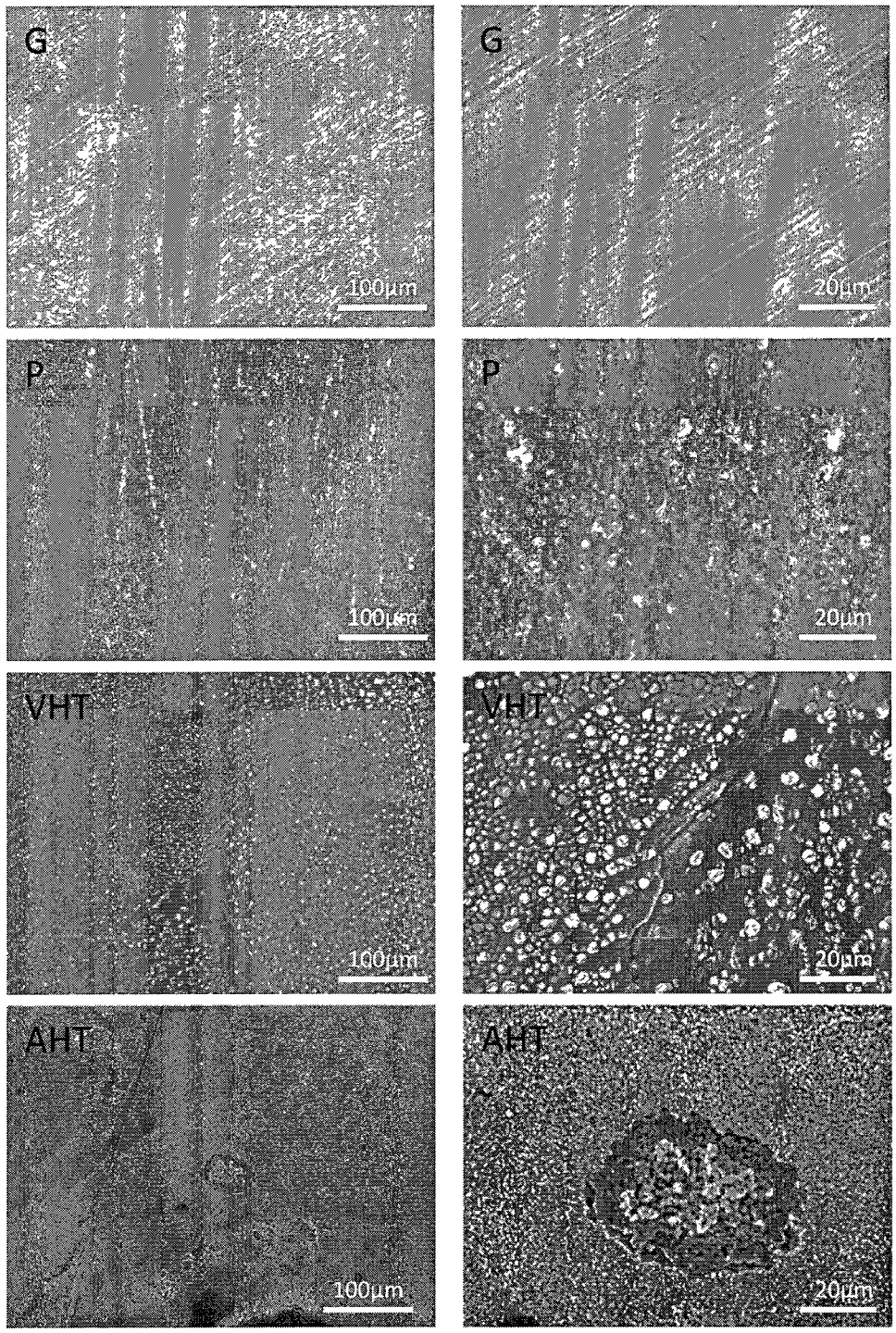

Figure 5-13 SEM images (Left: Low Mag., Right: High Mag.) of Ni20Cr5Al samples after 940 h SCW exposure.

5.3.2.5 Ni20Cr10AlY

Ni20Cr10AlY samples, similar to Ni20Cr5Al, also exhibited an adequate corrosion resistance after being exposed to SCW for 940 hours. Some oxides can be detected on both ground and polished samples, as shown in Figure 5-14. More Cr-enrichment was detected on the ground sample by EDS analysis (Table 5-6). For the vacuum heat treated sample, the surface contained discrete Al rich particles, likely to be alumina. Otherwise, increased Ni content was detected on the vacuum heat treatment sample, suggesting NiO formation as well. Additionally, yttrium was noticeably present on the vacuum heat treated sample (Y is known to promote oxide film adhesion to the substrate). As for air furnace heat treated sample, two elevations can be seen. The upper layer consisted of more Cr and Al enrichment than the lower layer. It is possible that the upper layer spalled off during heat treatment revealing the lower layer which was only Cr-enriched.

Table 5-6 EDS surface analysis results for Ni20Cr10AlY sample after 940h SCW exposure (wt%).

Ni20Cr10AlY	Cr	Al	Ni	Y	O
Ground	21.67	6.59	56.33	-	15.41
	25.62	7.79	66.59	-	0*
Polished	13.14	7.33	45.89	-	33.64
	19.80	11.05	69.15	-	0*
Vacuum H/T	2.82	6.97	49.16	3.16	37.89
	4.54	11.22	79.15	5.09	0*
Air Furnace H/T (lower layer)	23.07	6.44	57.26	-	13.23
	26.59	7.42	65.99	-	0*
Air Furnace H/T (upper layer)	25.82	13.10	26.33	-	34.75
	39.57	20.08	40.35	-	0*

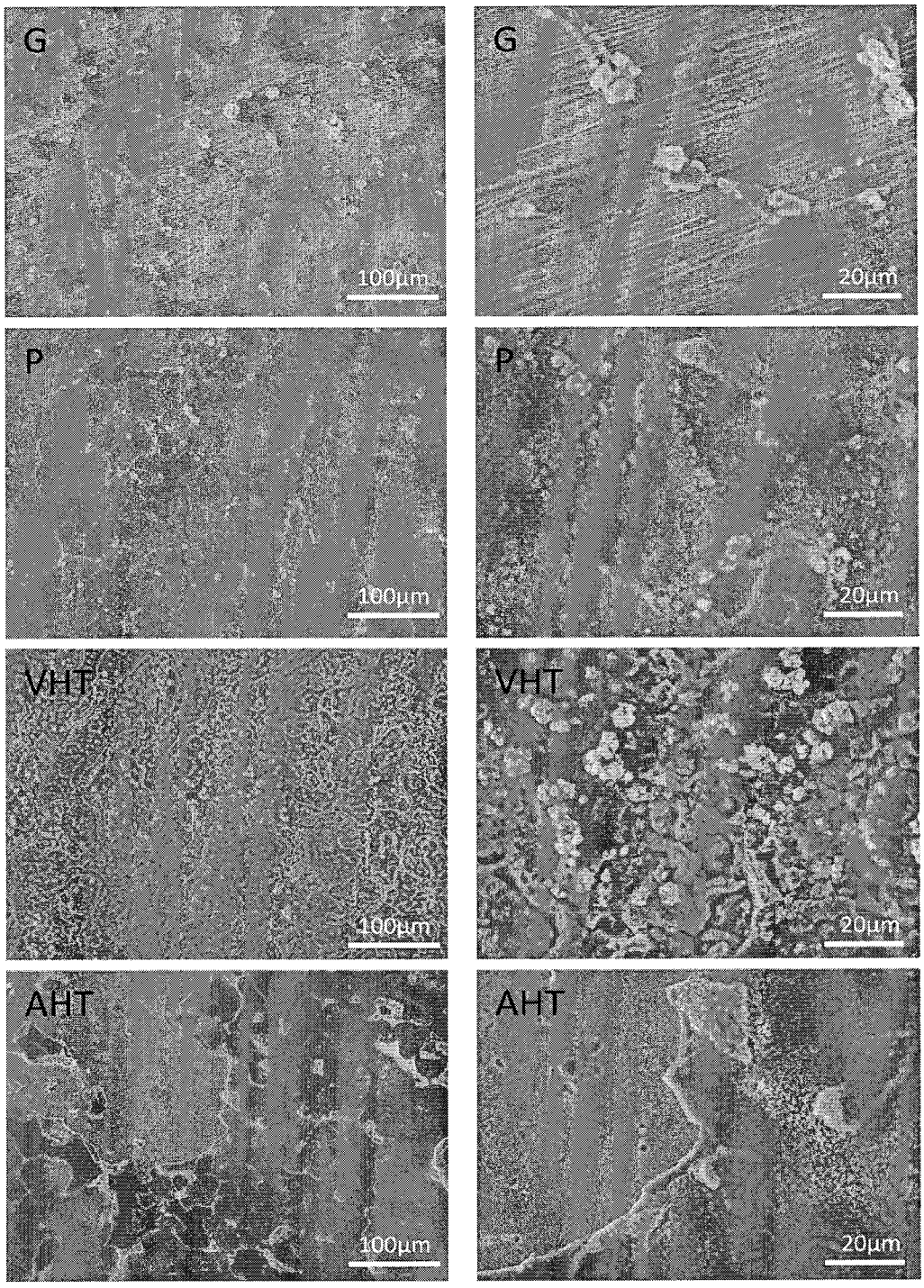

Figure 5-14 SEM images (Left: Low Mag., Right: High Mag.) of Ni20Cr10AlY samples after 940 h SCW exposure.

5.4 Visual Appearance of IN 625, 304 SS and NiCrAlY Coated Samples after SCW Testing

For the ground stainless steel 304 sample, the surface after testing showed grayish hue and occasional scale formation on the right lower side (Figure 5-15). For polished 304 SS sample, the surface appeared to have heavy, grainy scale and scale spalling was observed. In contrast, the uncoated IN 625 specimens showed much less scale formation. The ground IN 625 sample showed blue and grayish discoloration while the polished IN 625 had blue tint. Figure 5-15 illustrates the surface appearance of bare samples after testing.

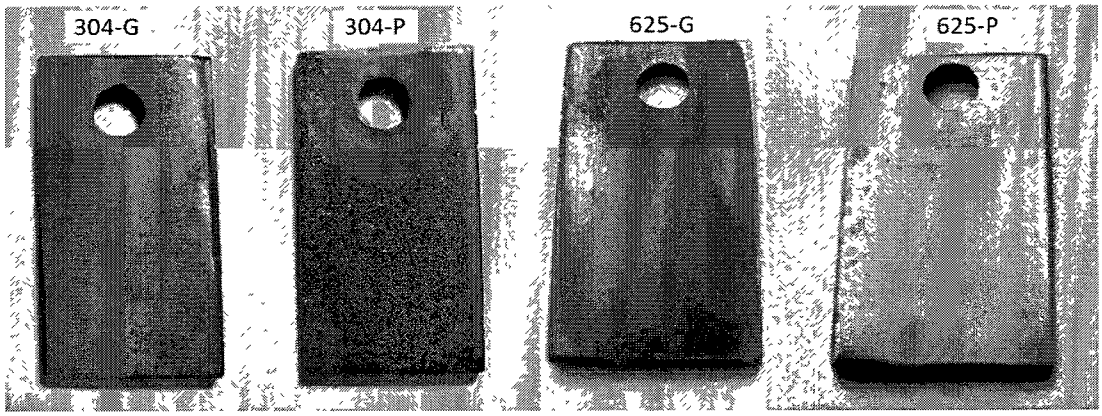

Figure 5-15 Visual appearance of bare 304 SS and IN 625 (10 mm x 20 mm) after 940hrs SCW testing.

After 500 hour testing in the supercritical water, the NiCrAlY coating evidently exhibited better corrosion resistance by observing the tested samples after 500 and 940 hr testing (Figure 5-16 and Figure 5-17). No obvious difference was found between ground and polished NiCrAlY coatings; however, the air heat-treated (HT) sample displayed greenish color due to the formation of oxide (NiO) during prior heat treatment process. The

exposure to SCW did not change the surface appearance of the heat treated NiCrAlY. Also, there was no difference between NiCrAlY coatings applied to 304 SS or IN 625.

After a total of 940 hour test, the scale on the NiCrAlY seems to have thickened somewhat by comparing the surface shades (Figure 5-17). Both ground and polished NiCrAlY samples became darker and the NiCrAlY coated 304 SS changed from blue hue to grayish color indicating further oxide formation. The heat treated NiCrAlY on IN 625 had the least change in surface appearance.

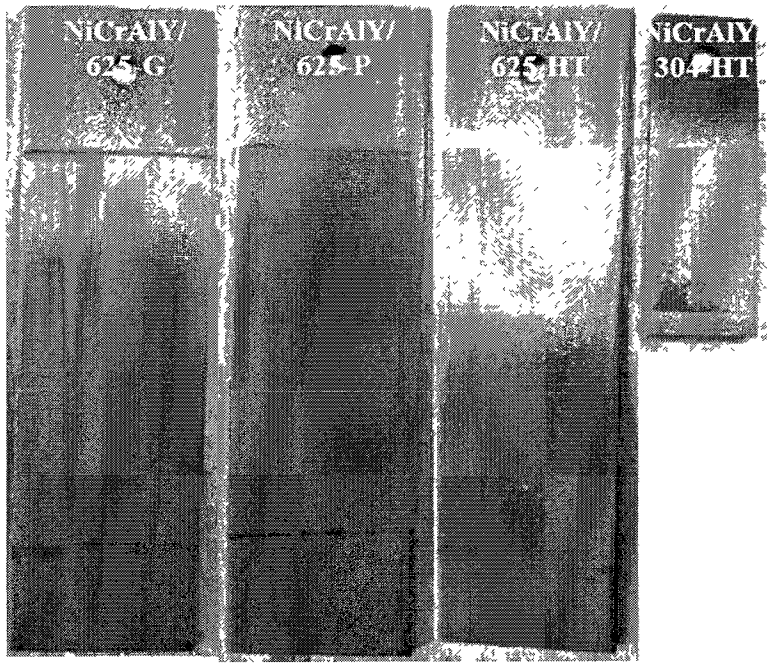

Figure 5-16 Coated samples after 500 hr test.

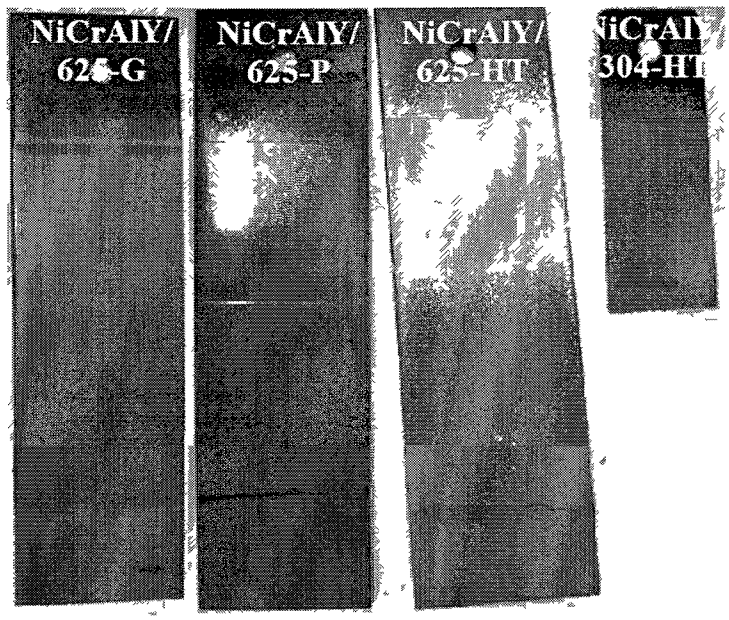

Figure 5-17 Coated samples after 940 hr test.

5.5 Weight Change Chart of IN 625, 304 SS and NiCrAlY Coated Samples after SCW Testing

The results of weight change for each stage and for a cumulative of 940 hours are shown in Table 5-7 and Figure 5-18. For the uncoated samples, the polished 304 SS saw some weight change while both the polished and ground IN 625 did not show noticeable weight change (Figure 5-18). The ground 304 showed less weight change than polished 304 – an observation consistent with our previous finding for the ground button samples. There was not much difference in the 500 hour and 940 hour tested samples in terms of weight change.

For the NiCrAlY coated samples, it is imperative to mention that the weight change reflected the total weight change from several different surfaces on a single sample: as-

coated areas at one end of the sample, coated and polished area in the center of the coated area (see Figure 4-2), and bare substrate surfaces on the back side. As such the trend observed on the weight change must be viewed with consideration of all surfaces in a qualitative manner as opposed to quantitative way.

Weight gain was observed for ground and polished NiCrAlY coated IN 625, the weight change was higher during stage 1 of the test. For the heat treated NiCrAlY sample, however, much less weight gain was observed illustrating the beneficial effect of oxidation heat treatment in inducing alumina and chromia formation. While all three NiCrAlY coated IN 625 samples contained various surfaces (coated, polished and uncoated), they were all similar in this respect. As such, it may be stated that heat treatment was beneficial for improving the corrosion resistance of NiCrAlY coating on IN 625.

For NiCrAlY coated 304 SS, it was the only sample in this group that suffered weight loss even thought the best surface condition (air heat treatment) was used. The weight loss in stage 2 was slightly less than the first stage. The weight loss on the NiCrAlY coated 304 SS sample was believed to have been resulted from scale spallation from the uncoated surfaces of this sample. SEM analysis will further elucidate this speculation.

Table 5-7 Weight change of each stage in run of NiCrAlY samples.

Sample No.	Initial weight (g)	Weight after 1st 500 hr (g)	Weight after 2nd 940 hr (g)	Surface area (dm^2)
304-G	2.4096	2.4099	2.4099	0.0478
304-P	2.4038	2.4043	2.4049	0.0478
625-G	2.4232	2.4233	2.4234	0.0478
625-P	2.2458	2.2458	2.2458	0.0478
NiCrAlY/304-HT	5.1740	5.1533	5.1528	0.0862
NiCrAlY/625-G	17.5287	17.5704	17.5867	0.3022
NiCrAlY/625-P	17.1982	17.2386	17.2539	0.3022
NiCrAlY/625-HT	17.4829	17.4901	17.4991	0.3022

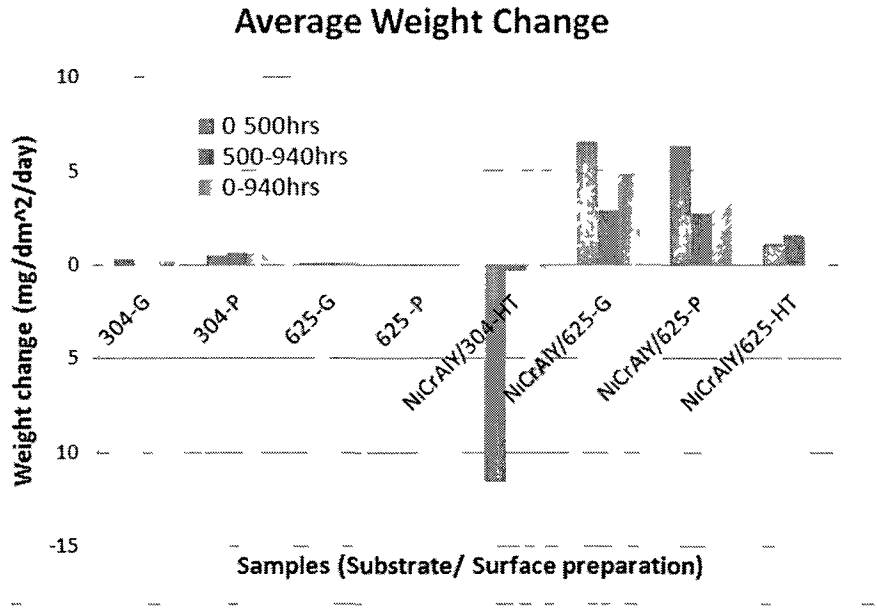

Figure 5-18 Average weight change for IN625, 304SS and NiCrAlY coated samples.

5.6 SEM Analysis Results of Bare and NiCrAlY Coated IN 625, 304 SS Samples after SCW Testing

5.6.1 SEM and EDS Analysis of Substrate Samples

SEM and EDS analysis was used to analyze the surface morphology and chemical composition of the bare samples after the second stage of testing in SCW. For ground 304, the majority of the surface still had the grinding marks (Figure 5-19, insert A) and a small portion of the surface showed new phase formation (see insert B and C of Figure 5-19). These phases had distinct features. The needle- and blocky-shaped bright phases shown in insert B had an elevated amount of oxygen and Fe and are most likely iron oxide (magnetite or hematite). The small cellular shaped phase shown in insert C had a higher Cr content and was likely to be a spinel phase.

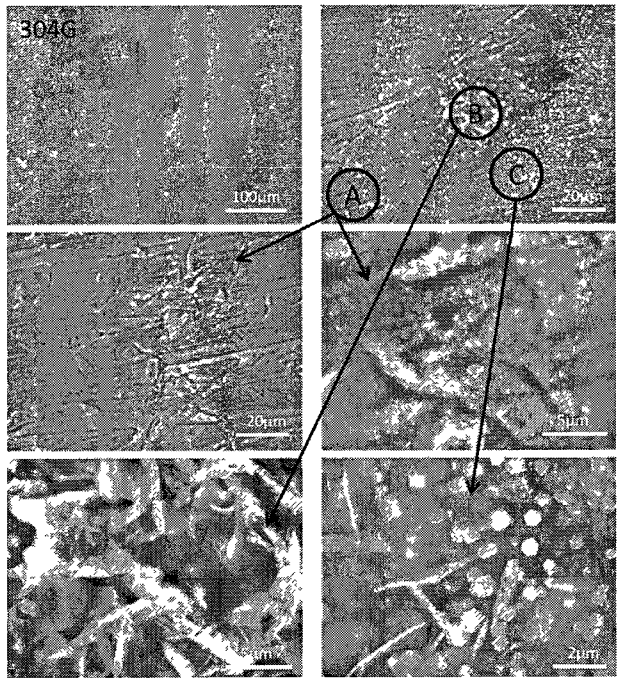

Figure 5-19 SEM analysis of ground 304 SS samples after 940hr SCW exposure.

The polished 304 SS sample had more surface scale formation than that found on the ground sample. No Cr-rich oxide was observed and most of the needle-like (insert A) and blocky-shaped phases (insert B) were likely to be Fe oxide based on the EDS analysis (Table 5-8). The phase shown in insert C (Figure 5-20) is a Si-containing compound formed occasionally from the condensation of dissolved silicone grease.

Table 5-8 EDS results of ground and polished 304 SS samples after 940hr SCW exposure (wt%).

EDS		O	Al	Cr	Fe	Ni	Si	Mn
304G	B	47.38	-	5.03	44.16	2.81	0.27	0.36
		0*	-	9.55	83.92	5.34	0.52	0.69
	C	23.76	1.00	17.91	51.21	3.58	1.26	1.27
		0*	1.31	23.50	67.17	4.69	1.65	1.66
304P	A & B	22.76	1.34	4.16	67.56	-	4.20	-
		0*	1.73	5.38	87.46	-	5.44	-
	C	51.41	4.16	2.43	25.69	5.68	10.29	0.35
		0*	8.56	4.99	52.88	11.68	21.18	0.71

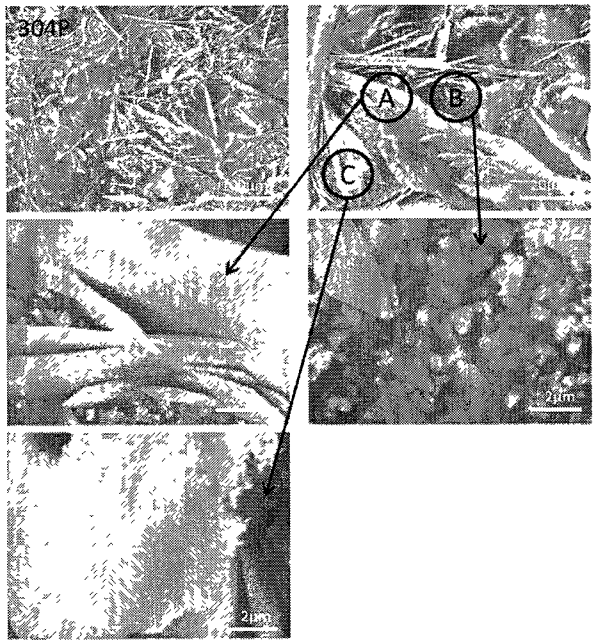

Figure 5-20 SEM images of polished 304 SS samples after 940 hr SCW exposure.

On the tested IN 625 surface (Figure 5-21 and Figure 5-22), there is no noticeable phase formation other than occasionally patches of light feathery particles which had been found to be a Si-containing compound from silicone grease. From a compositional point of view, the surfaces after SCW exposure showed increased oxygen content suggesting possible Chromia or NiO formation after the testing (Table 5-9). In comparison to the surfaces on 304 SS, IN 625 had very little change from the as-polished or as-ground state. The minimal weight change observed in Figure 5-18 confirmed that IN 625 indeed had better corrosion resistance than that of 304 stainless steel under the test conditions used in this study.

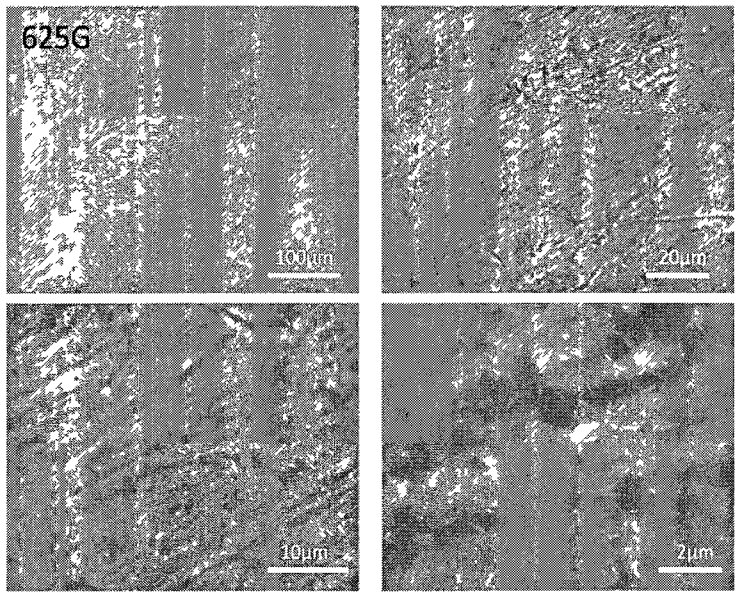

Figure 5-21 SEM analysis of ground IN 625 samples after 940hr SCW exposure.

Table 5-9 EDS results of ground and polished IN 625 samples after 940hr SCW exposure (wt%).

EDS	O	Al	Cr	Fe	Ni	Si	Mo	Nb
625G	26.75	1.07	17.82	4.01	38.67	2.80	6.34	2.54
	0*	1.46	24.33	5.47	52.79	3.82	8.65	3.46
625P	10.52	0.65	20.41	3.97	51.82	0.67	8.56	3.39
	0*	0.73	22.81	4.44	57.91	0.75	9.56	3.79

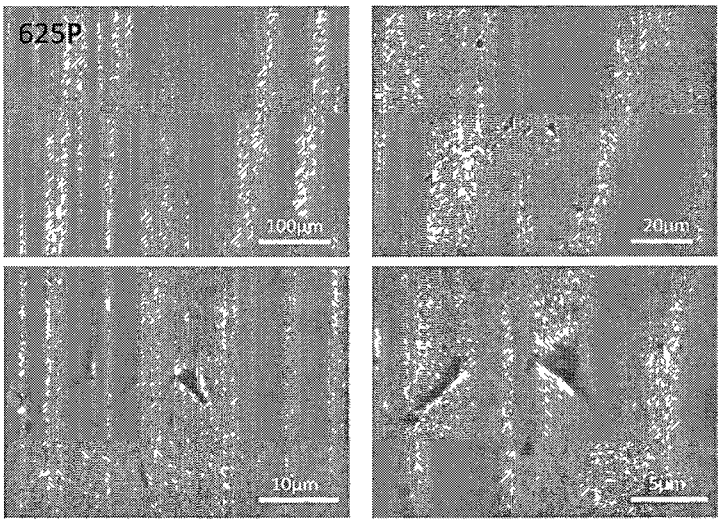

Figure 5-22 SEM images of polished IN 625 samples after 940hr SCW exposure.

5.6.2 SEM and EDS Analysis of Substrate on Coated Samples

On the non-coated surface areas (grit blasted condition for the preparation of plasma spray) surrounding the NiCrAlY coating (bottom of the sample and back side), corrosion was much more severe than the coated region. The surface became quite rough and more corrosion was believed to have taken place (Figure 5-23). On the bare surface of the non-heat treated IN 625 samples (beside ground or polished NiCrAlY), grit blasted (faceted) surface features were observed suggesting limited corrosion/oxidation. On the grit blasted and heat treated bare IN 625, visible oxide scale could be found on the surface. EDS analysis (Table 5-10) indicated the Cr content was much higher on the heat treated IN 625 as Cr_2O_3 formation must have occurred during heat treatment (Table 5-10, see highlighted elemental percentages). For bare 304 SS adjacent to the NiCrAlY coated region and in the heat treated condition, the oxides scale was found to spall off after 2nd stage testing in SCW by visual inspection. Additionally, the surface also suffered from apparent intergranular corrosion (IC) as shown in Figure 5-23. The grain boundaries were

attacked severely, while at the same time, fibre-like particles formed on the surface. EDS analysis (Table 5-10) suggests that they are iron oxide(s) in nature.

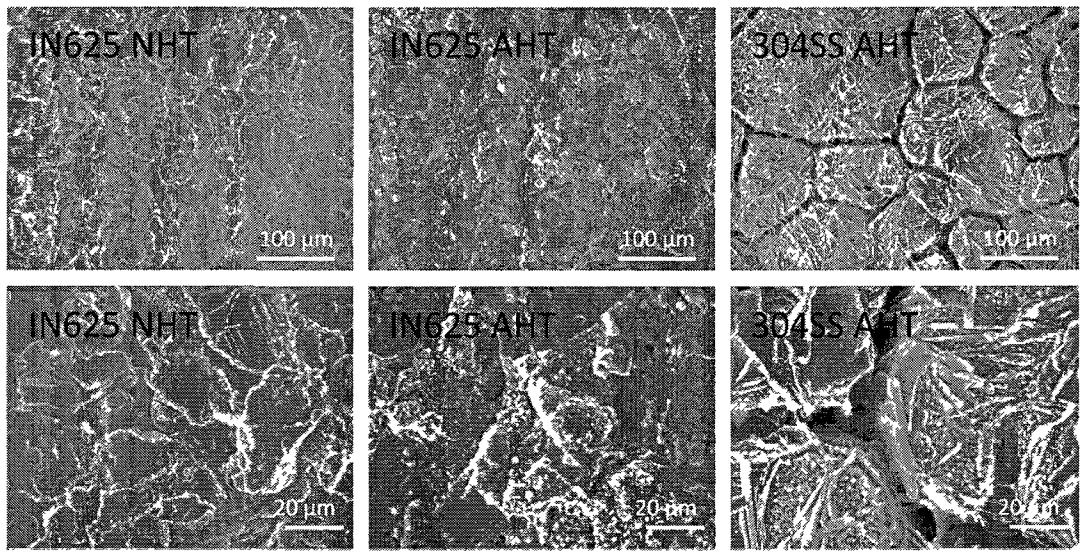

Figure 5-23 SEM images of substrate surfaces adjacent to NiCrAlY coating after 940hr SCW exposure (NHT: non-heat- treated, AHT: air-heat-treated).

Table 5-10 EDS results of substrate surfaces beside NiCrAlY Coating after 940hr SCW exposure (wt%).

EDS	O	Al	Cr	Ni	Fe	Mo	Ti	Mn	Nb	P
IN625 NHT	20.22	4.61	16.79	49.07	4.61	4.70	-	-	-	-
	0*	5.78	21.04	61.51	5.78	5.89	-	-	-	-
IN625 AHT	29.42	1.25	47.49	12.47	3.11	-	0.70	3.37	2.19	-
	0*	1.77	67.29	17.66	4.40	-	1.00	4.77	3.11	-
304SS AHT	26.75	-	2.36	-	70.47	-	-	-	-	0.42
	0*	-	3.23	-	96.20	-	-	-	-	0.57

5.6.3 SEM and EDS Analysis of As-Coated NiCrAlY

There was no noticeable morphological differences on the as-sprayed NiCrAlY surface (non-heat treated and heat treated) surrounding the polished and ground region of NiCrAlY on IN 625 and 304SS (Figure 5-24). The surface resembles the as-sprayed surface prior to SCW testing although higher oxygen content on the surface was detected by EDS analysis, indicating oxidation taking place during SCW testing. One noticeable difference between the heat treated and non-heat treated samples was the elevated Al percentage on the heat treated samples, suggesting alumina formation during heat treatment. Since heat treated sample (NiCrAlY on IN 625) exhibited a smaller weight change than non-heat treated sample (NiCrAlY on IN 625), alumina formation on the surface has contributed to slower weigh gain during SCW exposure.

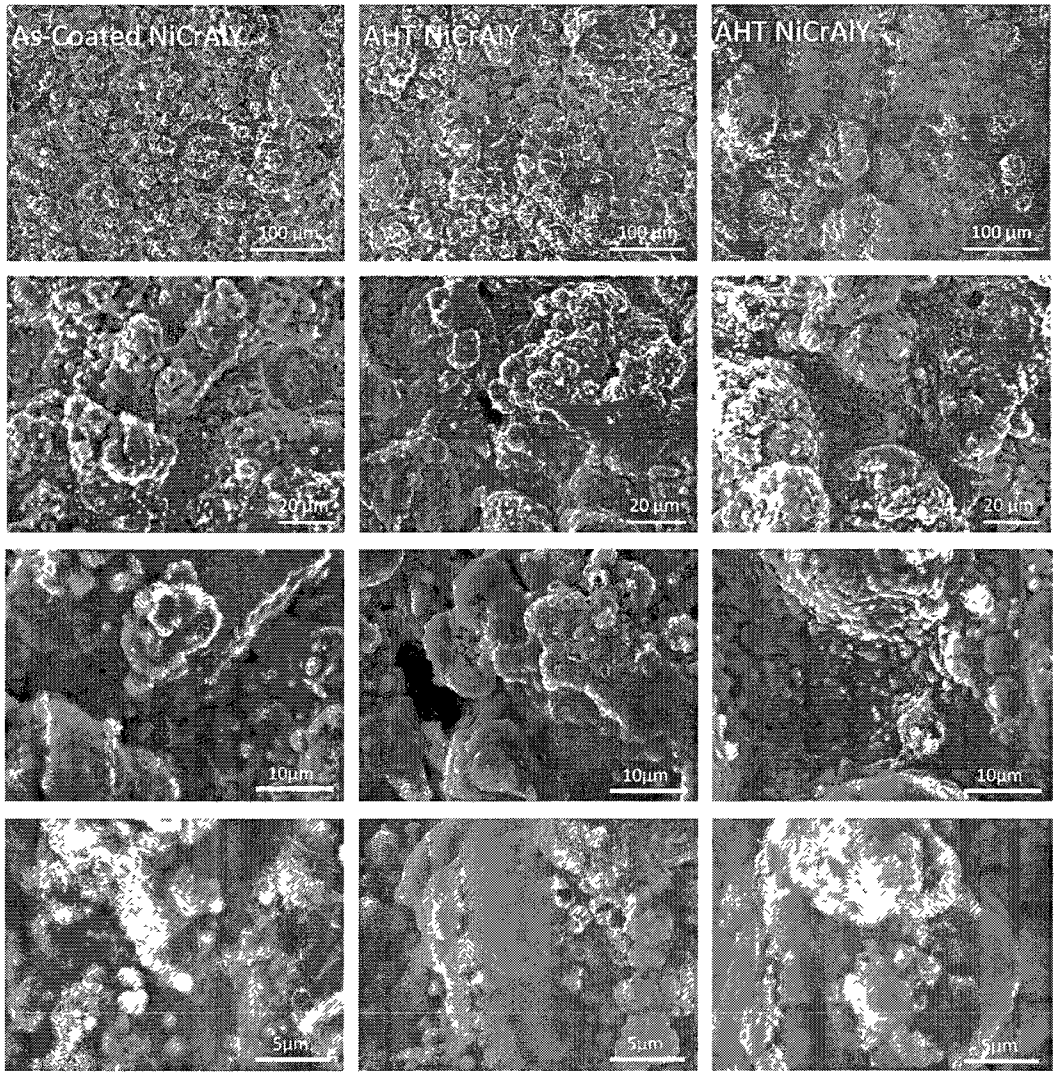

(a) On IN 625 (b) On IN 625 (c) On 304 SS

Figure 5-24 SEM image of as-coated region after 940hr SCW exposure.

Table 5-11 EDS results of as-coated NiCrAlY region after 940hr SCW exposure (wt%).

EDS	O	Al	Cr	Ni	Fe	Mn
NiCrAlY – As coated (on IN 625)	30.25	7.65	14.27	45.96	1.87	-
	0*	10.97	20.46	65.89	2.68	-
NiCrAlY – As coated and HT (on IN 625)	36.76	22.13	13.74	27.37	-	-
	0*	34.99	21.73	43.28	-	-
NiCrAlY – As coated and HT(on 304 SS)	34.11	18.01	16.45	28.54	1.70	1.19
	0*	27.34	24.96	43.31	2.59	1.80

5.6.4 SEM and EDS Analysis of Ground and Polished NiCrAlY On IN 625

The surface of the ground NiCrAlY on IN 625 still maintained the grinding marks as shown in Figure 5-25. Some oxidation may have taken place as EDS detected a strong oxygen signal from the surface of insert B (Figure 5-25). Occasional white clusters of particles were observed (insert A of Figure 5-25) and these particles were identified as a Si-containing compound (Table 5-12).

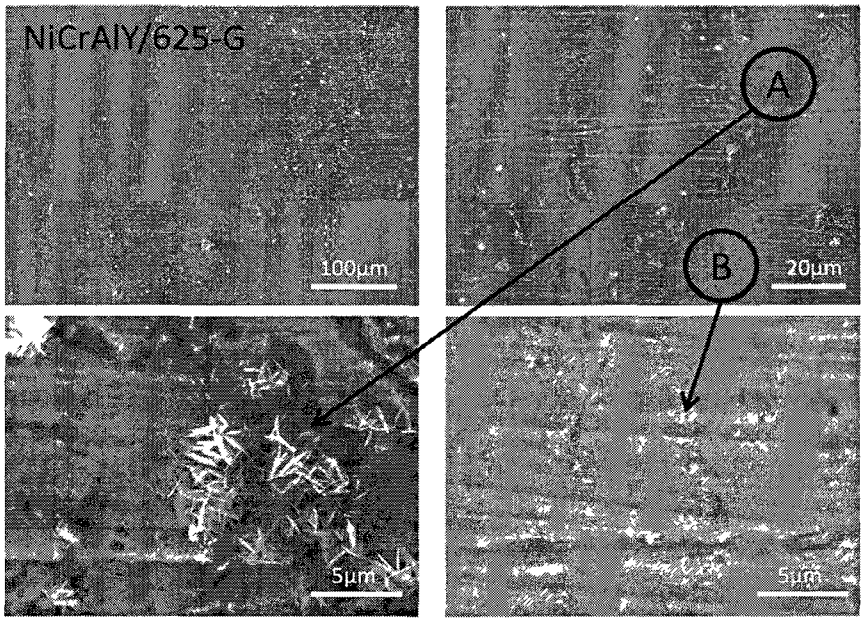

Figure 5-25 SEM image of ground NiCrAlY on IN 625 after 940hr SCW exposure.

Table 5-12 EDS results of ground and polished NiCrAlY on IN 625 after 940hr SCW exposure (wt%).

EDS		O	Al	Cr	Fe	Ni	Si
NiCrAlY/625-G	A	45.09	6.40	4.19	5.50	22.86	15.96
		0*	11.66	7.63	10.02	41.64	29.07
	B	15.57	8.08	18.34	0.91	55.25	1.85
		0*	9.57	21.73	1.07	65.43	2.19
NiCrAlY/625-P	A(fibre)	41.60	4.33	7.22	5.56	26.74	14.55
		0*	7.41	12.37	9.53	45.79	24.92
	A (ball)	42.75	2.76	3.79	2.41	43.10	5.19
		0*	4.82	6.62	4.21	75.28	9.07
	B	12.04	8.51	18.63	0.52	59.39	0.91
		0*	9.67	21.18	0.59	67.52	1.03

On the polished NiCrAlY surface, the typical plasma sprayed features (splats, un-melted particles and oxide stringers) were still visible (insert B of Figure 5-26). EDS analysis found the presence of oxygen, indicating oxidation has taken place during SCW testing. Again, clusters of while Si-containing compounds were found. On both ground and polished surfaces, no corrosion pits or scale spalling were observed.

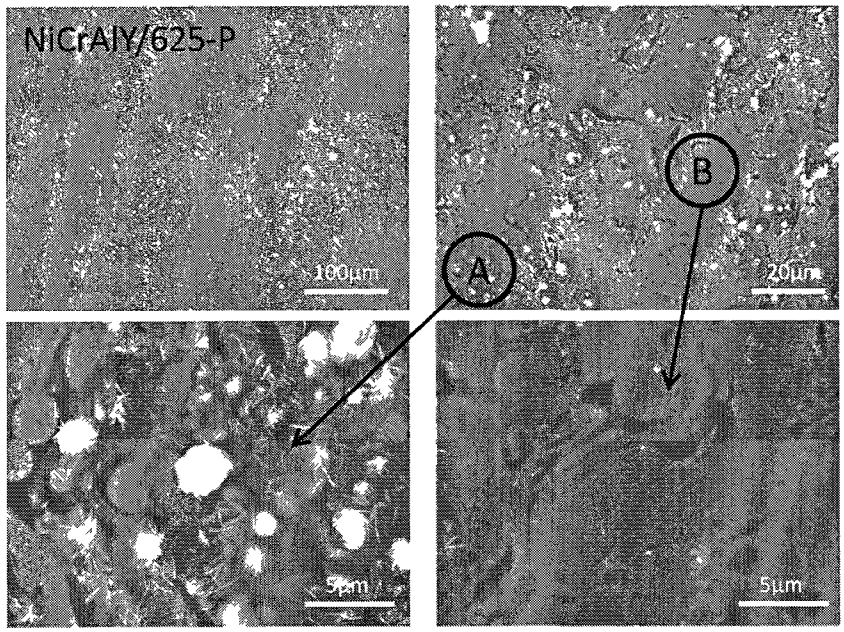

Figure 5-26 SEM images of polished NiCrAlY on IN 625 after 940hr SCW exposure.

5.6.5 SEM and EDS Analysis of Heat Treated NiCrAlY on IN 625 and 304 SS

The heat treated NiCrAlY coating samples (on both IN 625 and 304 SS) were covered with fine oxide layer that was believed to be mainly alumina judging from the EDS results given in Table 5-13. Also observed from the EDS analysis was the higher Al content (lower Cr content) on the heat treated surfaces (insert A of Figure 5-27 and insert A and B of Figure 5-28) suggesting alumina formation during heat treatment. Some isolated Cr-rich oxide (insert B in Figure 5-28) and Ni and Cr-rich oxide (insert C in Figure 5-28) were also found on the heat treated surface after SCW exposure.

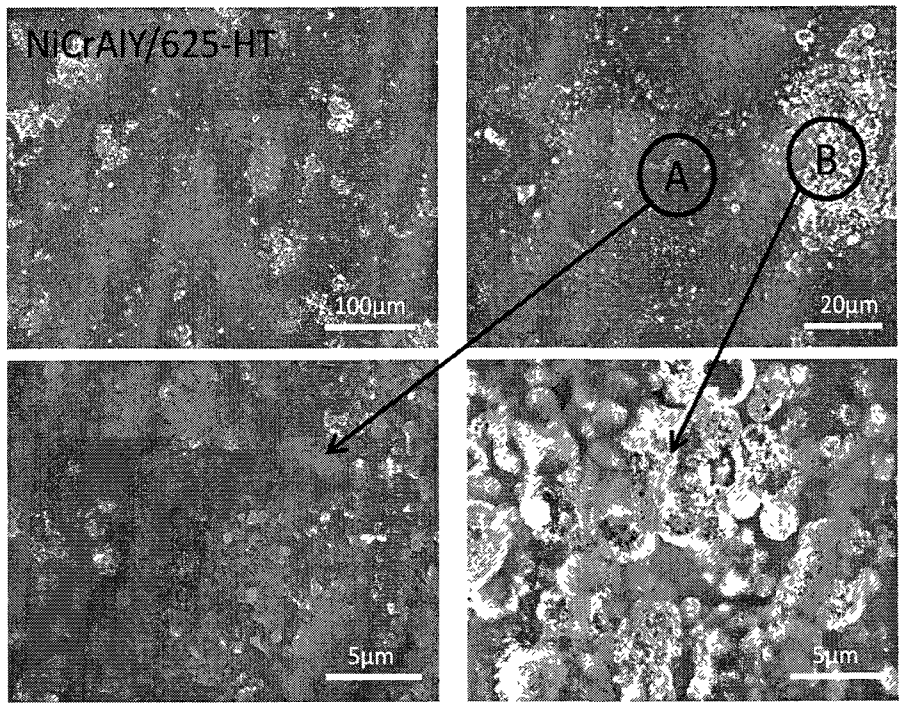

Figure 5-27 SEM images of heat treated NiCrAlY on IN 625 after 940hr SCW exposure.

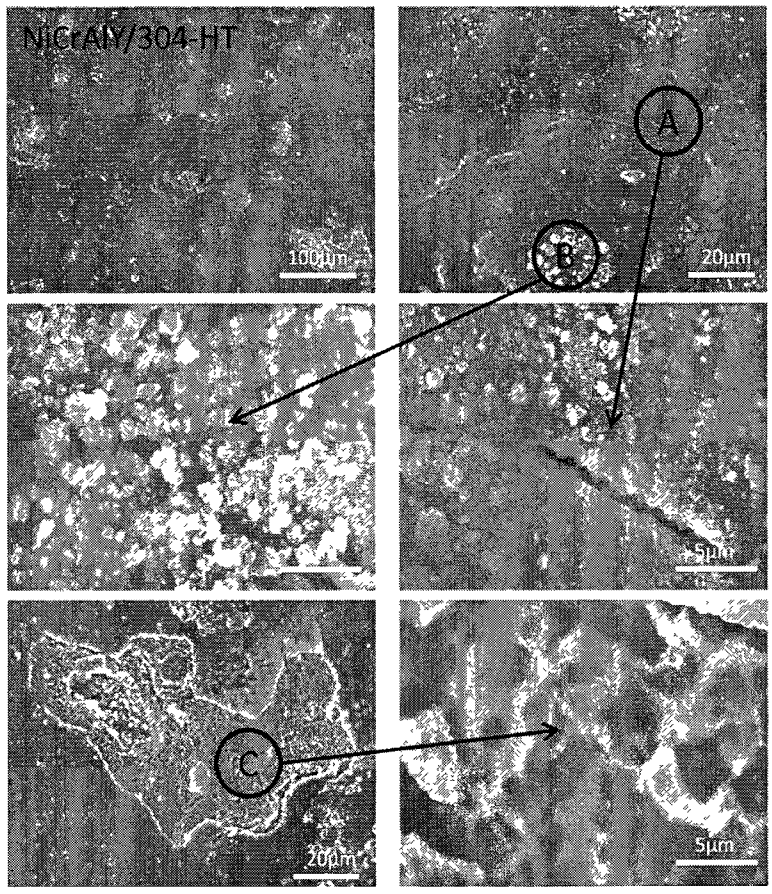

Figure 5-28 SEM analysis of heat treated NiCrAlY coating (on 304 SS) after 940hr SCW exposure.

Table 5-13 EDS results of heat treated NiCrAlY coating after 940hr SCW exposure (wt%).

EDS		O	Al	Cr	Fe	Ni	Si	Y
NiCrAlY/625-HT	A	40.21	34.02	7.30	0.49	17.97	-	-
		0*	56.90	12.21	0.82	30.06	-	-
	B	31.09	4.83	24.35	2.21	35.16	2.35	-
		0*	7.01	35.34	3.21	51.01	3.42	-
NiCrAlY/304-HT	A	43.30	38.28	5.55	0.36	11.56	-	0.95
		0*	67.51	9.79	0.64	20.38	-	1.68
	B	39.82	32.84	7.85	0.36	18.07	-	1.04
		0*	54.56	13.05	0.61	30.03	-	1.73
	C	23.50	5.02	19.75	2.55	44.42	4.76	-
		0*	6.56	25.83	3.33	58.07	6.22	-

5.7 Summary

From the test results of bulk coating samples (button samples), the effects of composition and surface preparation method on the corrosion behavior of five Ni-based alloys were characterized. After 500 and 940 hours of corrosion testing in supercritical water at 500°C and a pressure of 27 MPa, samples ground with 600 grit sand paper and polished with alumina showed the least weight gain, and their surface morphologies were not affected appreciably by the SCW exposure. Vacuum furnace heat-treatment produced a very light surface oxide film and all samples showed moderate weight gain after testing. However, samples that were air furnace heat-treated formed surface scales and suffered weight loss (except Ni20Cr5Al). This weight loss observed could be attributed to the spalling of the oxides formed during heat treatment in air. Of all the samples tested, Ni20Cr5Al prepared with 600 grit sand paper showed the best performance with respect to weight change under the test condition used in this study. Ni20Cr10AlY also has the

potential to be a corrosion resistant coating composition, however, the Cr and Al segregation and presence of pores in the bulk sample may have undermined the corrosion performance of Ni20Cr10AlY alloy.

For the NiCrAlY coated and bare IN 625 and 304 SS samples, it was found that IN 625 was more resistant to corrosion in SCW than 304 SS based on visual observation, weight change and SEM analysis of the tested samples. Surface preparation method influenced the weight change of 304 SS samples more than that of IN 625 samples. The NiCrAlY coating showed excellent corrosion resistance in general and the heat treated NiCrAlY had even greater corrosion resistance due to the formation of alumina on the surface. The heat treated NiCrAlY on IN 625 sample had the least weight gain among the coated samples. NiCrAlY coated 304 SS was the only coated sample that had substantial weight loss and most of this weight loss occurred on the bare 304 SS surfaces surrounding NiCrAlY coating.

6. Conclusions and Suggested Future Work

Currently, there is very little work focused on the corrosion behaviour of coatings in SCW. This study showed that Al and Cr in combination offered better corrosion resistance (than Al or Cr acts alone) in SCW. Secondly, it was for the first time that the effect of surface conditions was systematically studied. Furthermore, plasma sprayed NiCrAlY coating was tested for the first in SCW and the good corrosion protection was observed. Lastly, the combination of NiCrAlY and exposed 304 SS was found not suitable to be used in SCW due to the accelerated corrosion.

In this research, two supercritical water systems were set up. Following preliminary tests and trouble shooting of the systems, several nickel based coating materials and NiCrAlY plasma coated IN 625 and 304 SS samples were tested in the SCW systems. All samples were prepared using various surface preparation methods (grinding, polishing, air heat treatment and vacuum heat treatment) prior to being tested in SCW for about 940 hours in two stages. The samples before and after SCW test were analyzed using SEM/EDS. Based on the results obtained, the following conclusions can be drawn:

- A combination of Al and Cr will likely be needed in order to improve the corrosion resistance of Ni-based alloys when being exposed to SCW.
- Surface preparation methods significantly influence the corrosion behaviour of samples during SCW exposure. Grinding offers the best results in terms of weight gain and surface morphology.
- IN 625 has better corrosion resistance than 304 SS under SCW condition used in this study.

- NiCrAlY plasma coating shows superior corrosion resistance to IN 625 and 304 SS based on visual and SEM analysis.
- Heat treatment of Al and Cr containing nickel based alloys promotes the formation of alumina and chromia which could be beneficial to corrosion resistance in SCW.
- The presence of plasma sprayed NiCrAlY coating on 304 SS accelerates the corrosion of 304SS due to the galvanic corrosion.

Based on the information generated in this study, the following recommendations are made:

- Further evaluation of test samples for detailed oxide formation after SCW exposure. Due to the thin nature of the oxide formed during SCW exposure, traditional SEM/EDS was not able to identify the type and thickness of the oxides formed. Preliminary STEM/FIB work carried out at NRCan/CANMET showed more detail oxide structure consisting of outer layer of Fe-rich oxide and inner layer of Ni-rich oxide on bare 304 SS after SCW test. More samples will be analyzed using this tool.
- Long term test needs to be carried out to study the corrosion behaviour in steady-state. Currently, NiCrAlY samples are being tested for up to 5000 hours.
- Conduct tests under different water densities. As discussed previously, water density can vary within the supercritical regime and dissolved ionic products change significantly with the water density. As such, corrosion performance of samples with various compositions should be studied under different density settings.
- Develop plasma spray coating process to coat all surfaces of the sample. This way the true performance of the coating can be evaluated.

Appendices

Appendix A

Information of NiCrAlY Powder

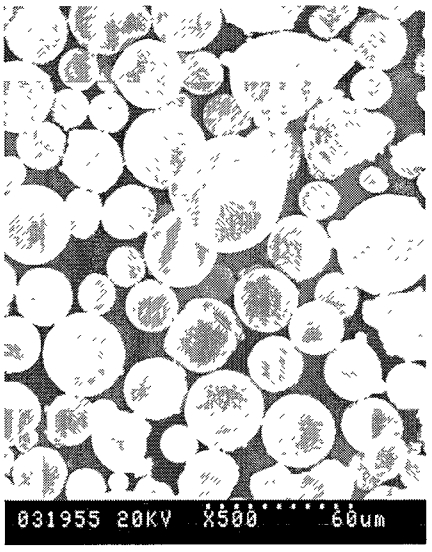

SEM Image of As-Received NI-343 NiCrAlY Powder

Powder Specification

	Nominal Chemistry	Powder Name	Flow Density	Size	OEM Specs/ Trade Names	Application Data
Ni-22Cr-10Al-1Y Atomized	Cr 22 0 Al 10 0 Y 1 0 Ni Rem	NI-164/ NI-211	20 sec 3 6 g/cm^3	-140/+270 mesh -106 µm/+53 µm	B50TF162 CLA B50TF192 CLA DMR 33 090 B50A892	• Good diffusional stability and oxidation properties • Useful up to 1800°F (982°C) • Typically used for a TBC bondcoat
		NI-211-2	20 sec 3.6 7g/cm^3		B50AG16 CLA	
		NI-211-4	17 sec 3 70 g/cm^3		B50AG16 CLB	
		NI-211-7	21 sec 3 60 g/cm^3		B50AG16 CLE	
		NI-211-17	17 sec 3.73 g/cm^3		B50AG16 CLD	
		NI-164-2	17 sec 3 8 g/cm^3	-200/+325 mesh -75 µm/+45 µm	EMS 57737 II	
		NI-343	neg 3 8 g/cm^3	-325 mesh/+10 µm -45 µm/+10 µm		

(Ref. Powder Solutions Catalog, PRAXAIR Surface Technologies, 2009)

Appendix B

SEM/FIB/STEM images of 304SS

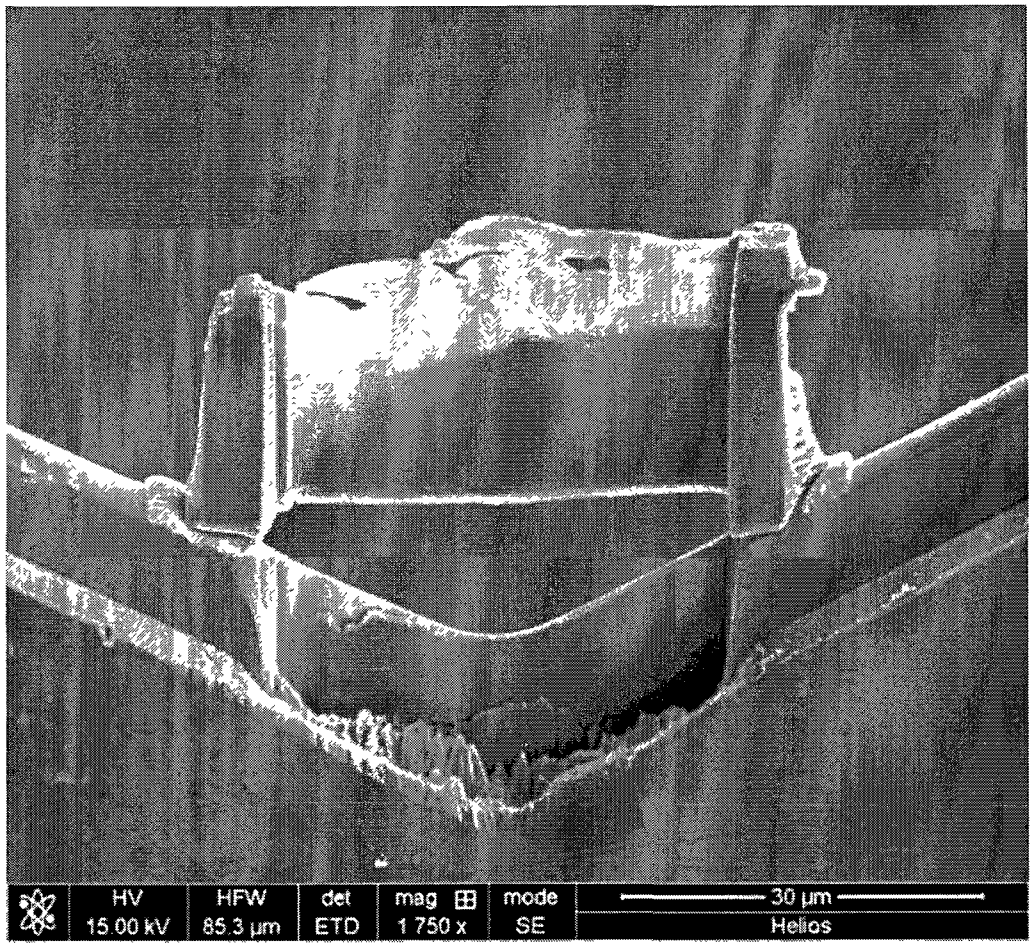

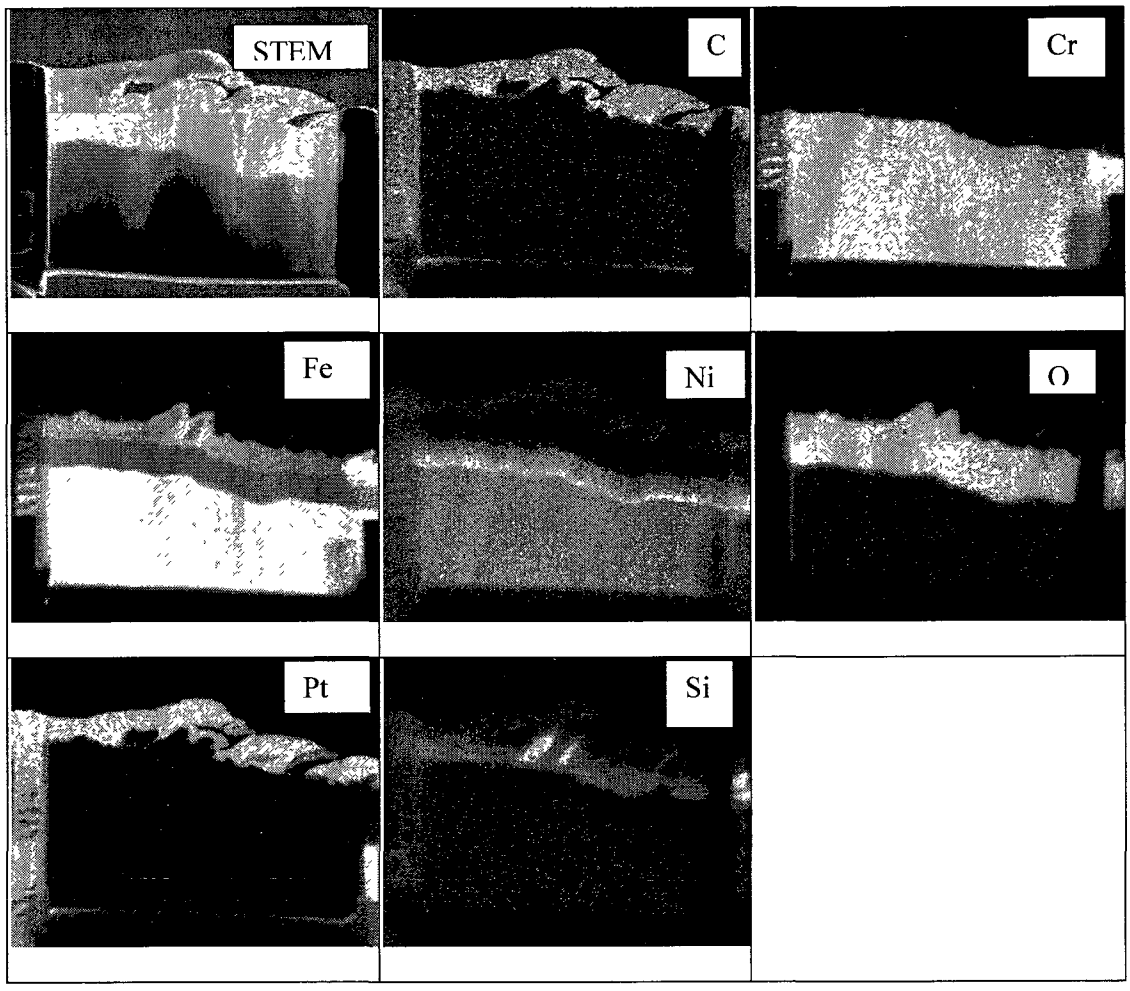
STEM
C
Cr
Fe
Ni
O
Pt
Si

Appendix C

Plasma Spray Report Sheet

Axial III System Run Time Report

Product Name	NI-343	Nozzle	12slm
Recipe Name	T21-4	Distance	40 m mm
Date	15-Jun-10	Time	12 07 30
Recipe Number	-1 00	Feeder	3 8
Operator	Carleton Unr. ersity	Passes	52g m

RECIPE:

Total Flow [slm]	Nitrogen [%]	Hydrogen [%]	Current [A]	Carrier [slm]	Feed [rpm]
230	**10.0**	**23.0**	**250**	**12.0**	**4.0**

GAS FLOW:

	Set Point	Value
Argon	400 0	156 8
Nitrogen	23 0	22 0
Hydrogen	52 9	52 2
Jet1	90 1	90 0
Jet2	90 1	59 5
Jet3	90 1	90 0
Total	**230.0**	**230.8**
Carrier	12.0	11 9
Shroud	0 0	0 0

WATER:

Flow	10 6
Temp In	10 6
Temp Out	31 1
Temp Diff	20 5

PRESSURE:

Jet1	27 1
Jet2	27 1
Jet3	26.1

POWER:

	Current		Voltage	Power	Enthalpy
	Set Point	Value			
Source1	250	251	137	34 2	10 6
Source2	250	251	140	35 1	11 0
Source3	250	251	139	34 7	10 8
Average:		**251**	**139**	**34.6**	**10.8**
Total:				**104.0**	

Control Mode:

Run Performed In Automanc Control Mode

Operators Comments:

End of Report

References

1. J. Kaneda, S. Kasahara, J. Kuniya, K.Moriya, F. Kano, N. Saito, A. Shioiri, T. Shibayama and H. Takahashi, "General corrosion properties of titanium based alloys for the fuel claddings in the supercritical water-cooled reactor", Proceedings of the 12th International Conference on Environmental Degradation of Materials in Nuclear Power System-Water Reactors, TMS, 2005.
2. D. Guzonas, "SCWR materials and chemistry status of ongoing research", GIF Symposium, Paris, France, Sept. 9-10, 2009.
3. D. Guzonas, J. Wills, H. Dole, J. Michel, S. Jang, M. Haycock and M. Chutumstid, "Steel corrosion in supercritical water: an assessment of the key parameters", Proceedings of the 2nd Canada-China Joint Workshop on Supercritical Water-Cooled Reactors (CCSC-2010), Toronto, ON, Canada, April 2010.
4. A Technology roadmap for generation IV nuclear energy systems, December 2002. http://www.gen-4.org/Technology/roadmap.htm
5. P. Kritzer, "Corrosion in high-temperature and supercritical water and aqueous solutions: a review", Journal of Supercritical Fluids, Vol.29 (2004), pp.1-29.
6. S. S. Hwang, B. H. Lee, J. G. Kim and J. Jang, "SCC and corrosion evaluations of the F/M steels for a supercritical water reactor", Journal of Nuclear Materials, Vol.372(2008), Iss.2-3, pp. 177-181.
7. IEA Statistics/Electricity and Heat by country http://www.iea.org/stats/electricitydata.asp?COUNTRY_CODE=29
8. 2009 GIF R&D Outlook for Generation IV Nuclear Energy Systems, August 2009.

http://www.gen-4.org/GIF/About/index.htm

9. K. Yamada, S. Sakurai, Y. Asanuma, R. Hamazaki, Y. Ishiwatari and K. Kitoh, "Overview of the Japanese SCWR concept developed under the GIF collaboration", Proceedings of the 5th International Symposium on Supercritical Water-Cooled Reactors (ISSCWR-5), March 13-16 2011, Vancouver BC, Canada
10. C.Sun, R.Hui, W.Qu, S.Yick, "Review: progress in corrosion resistant materials for supercritical water reactors", Corrosion Science, Vol.51 (2009), pp. 2508-2523.
11. J. E. Oakey, L. W. Pinder, R. Vanstone, M. Henderson, S. Osgerby, "Review of status of advanced materials for power generation," UK Department of Trade and Industry, Report No. COAL R224, February 2003.
12. G.Brunner, "Near and supercritical water. Part II: Oxidative Processes", the Journal of Supercritical Fluids, Vol.47 (2009), pp. 382-390.
13. Lu Dao-gang and Peng Chang-hong, "Review of supercritical water cooled reactor", Atomic Energy Science and Technology, Vol.43 (2009), No.8, pp. 743-749.
14. M. Kutz, "Supercritical Water Oxidation", Environmentally Conscious Materials and Chemical Processing, Chapter 13, John Wiley & Sons, 2007.
15. http://www.btinternet.com/~martin.chaplin/phase.html
16. R. B. Gupta, Supercritical Water Oxidation, in Encyclopedia of Chemical Processing, Marcel Dekker, November 2005.
17. L. B. Kriksunov and D. D. Macdonald, "Understanding chemical conditions in supercritical water oxidation systems", Proceedings of the ASME Heat Transfer Division, HTD-Vol. 317-2, IMECE, 1995.

18. M. C. Bellissent-Funel, "Structure of supercritical water", Journal of Molecular Liquids, Vol. 90 (2001), pp. 313-322.

19. V. Tulkki, "Supercritical water reactors", Master's Thesis, Helsinki University of Technology, November 2006.

20. M. Nakahara, N. Matubayasi, C. Wakai and Y. Tsujino, "Structure and dynamics of water: from ambient to supercritical", Journal of Molecular Liquids, Vol. 90 (2001), pp.75-83.

21. http://en.wikipedia.org/wiki/Hydrogen_bond

22. Chemistry Tutorial: the Chemistry of Water (Page 3), Department of Biochemistry and Molecular Biophysics, University of Arizona, 2003.

23. P. Postorlno, R. H. Tromp, M-A. Ricci, A. K. Soper and G. W. Neilson, "The interatomic structure of water at supercritical temperature", Nature, Vol. 366 (1993), pp. 668-670.

24. M. Nakahara, "The structure and properties of supercritical water", The Japan Society of Calorimetry and Thermal Analysis, Vol. 31 (2004), Issue 1, pp. 14-22.

25. P.Kritzer, N.Boukis and E.Dinjus, "Factors controlling corrosion in high-temperature aqueous solutions: a contribution to the dissociation and solubility data influencing corrosion process", Journal of Supercritical Fluids, Vol.15 (1999), pp.205-227.

26. M.L. Japas and E.U. Franck, "High pressure phase equilibria and PVT-data of the water-oxygen system including water-air to 673K and 250MPa", Ber Bunsenges Phys. Chem., Vol. 89 (12) (1985), pp.1268-1275.

27. W.G. Cook and R. Olive, "Pourbaix Diagrams for Iron, Nickel and Chromium in sub-critical and supercritical water", Proceedings of 2nd Canada-China joint Workshop on SCWRs (CCSC-2010), Toronto, 2010.

28. T. Adschiri, K. Sue, K. Aria and Y. Watanabe, "Estimation of metal oxide solubility and understanding corrosion in supercritical water", Corrosion 2001, NACE National Association of Corrosion Engineers, Houston, TX, Paper no.1354,2001.

29. P. Kritzer, N. Boukis and E. Dinjus, "Transpassive dissolution of alloy 625, chromium, nickel, and molybdenum in high-temperature solutions containing hydrochloric acid and oxygen", Corrosion, Vol. 56 (2000), pp. 265.

30. Y. Chen, K. Sridharan and T. Allen, "Corrosion behaviour of Ferritic-Martensitic steel T91 in supercritical water", Corrosion Science, Vol.48 (2006), pp. 2843-2854.

31. G. Was, P. Ampornrat, G. Gupta, S. Teysseyre, E. West, T. Allen, K. Sridharan, L. Tan, Y. Chen, X. Ren and C. Pister, "Corrosion and stress corrosion cracking in supercritical water", Journal of Nuclear Materials, Vol.371 (2007), pp.176-201 .

32. W. D. Callister Jr., Materials science and engineering: an introduction, 7th ed., p 345, New York, John Wiley & Sons Inc., 2007

33. K. L. Murty and I. Charit, "Structural materials for gen-IV nuclear reactors: challenges and opportunities," Journal of Nuclear Materials, Vol. 383 (1-2) (2008), pp. 189-95.,

34. K. Eherlich, J. Konys and L. Heikinheimo, "Materials for high performance light water reactors," Journal of Nuclear Materials, Vol. 327 (2-3) (2004), pp. 140-147.

35. Y. Chen, K. Sridharan and T.R. Allen, Corrosion 2005, Paper 05391, NACE International, Houston, TX, 2005.

36. L. Tan, K. Sridharan and T.R. Allen, "The effect of grain boundary engineering on the oxidation behavior of INCOLOY alloy 800H in supercritical water", Journal of Nuclear Materials, Vol. 348 (2006), pp. 263–271.

37. T. R. Allen, L. Tan, G. S. Was and E. A. Kenik, "Thermal and radiation-induced segregation in model Ni-base alloys," Journal of Nuclear Materials, Vol. 361 (2007), pp. 174-183.

38. A. Aguero, R. Muelas and V. Gonzalez, "HVOF coatings for steam oxidation protection," Materials and Corrosion, Vol. 59 (2008), pp. 393-401.

39. R. N. Durham, L. Singheiser and W. J. Quadakkers, "Identification of degradation mechanisms in coatings for supercritical steam applications," Materials and Corrosion, Vol. 59 (2008), pp. 402-408.

40. F. A. Khalid, N. Hussain and A. H. Qureshi, "Microstructural study on oxidation of aluminized coating on Inconel 625", Journal of Materials Engineering and Performance, Vol.11 (2) (2002), pp. 211-214.

41. Kohei Oda and Tetsuo Yoshi, "Hydrothermal corrosion of alumina ceramics", J. Am. Ceram. Soc., Vol. 80 (12) (1997), pp.3233-3236.

42. N. Boukis, N. Claussen, K. Ebert, R. Janssen and M. Schacht , "Corrosion screening tests of high-performance ceramics in supercritical water containing oxygen and hydrochloric acid", Journal of the European Ceramics Society, Vol. 17 (1997), pp. 71-76.

43. F. Gao, X. Huang, Q. Yang and R. Liu, "Optimization and prediction of plasma spray process by Taguchi method", Journal of Thermal Spray, accepted, Oct. 2011.

44. H. W. W. Wong, "Heat transfer analysis of the plasma spray deposition process", PhD thesis at UBC, 1997.

45. S. Saeidi, K. T. Voisey and D. G. McCartney, "The effect of heat treatment on the oxidation behavior of HVOF and VPS CoNiCrAlY coatings", Journal of Thermal Spray Technology, Vol. 18 (2009), pp. 209-215.

46. V. K. Tolpygo and D. R. Clarke, "The effect of oxidation pre-treatment on the cyclic life of EB-PVD thermal barrier coatings with platinum aluminide bond coats", Surface and Coatings Technology, Vol. 200 (2005), pp. 1276 – 1281.

47. H. Lau, C. Leyens, U. Schulz and C. Friedrich, "Influence of bond coat pre-treatment and surface topology on the lifetime of EB-PVD TBCs", Surface and Coatings Technology, Vol. 165 (2003), pp. 217–223.

48. B. Baufeld and U. Schulz, "Life time dependency on the pre-coating treatment of a thermal barrier coating under thermal cycling", Surface and Coatings Technology, Vol. 201 (2006), pp. 2667–2675.